A resonant sextuplet of sub-Neptunes transiting the bright star HD 110067

https://doi.org/10.1038/s41586-023-06692-3

Received: 2 May 2023

Accepted: 28 September 2023

Published online: 29 November 2023

Check for updates

Planets with radii between that of the Earth and Neptune (hereafter referred to as 'sub-Neptunes') are found in close-in orbits around more than half of all Sun-like stars[1,2]. However, their composition, formation and evolution remain poorly understood[3]. The study of multiplanetary systems offers an opportunity to investigate the outcomes of planet formation and evolution while controlling for initial conditions and environment. Those in resonance (with their orbital periods related by a ratio of small integers) are particularly valuable because they imply a system architecture practically unchanged since its birth. Here we present the observations of six transiting planets around the bright nearby star HD 110067. We find that the planets follow a chain of resonant orbits. A dynamical study of the innermost planet triplet allowed the prediction and later confirmation of the orbits of the rest of the planets in the system. The six planets are found to be sub-Neptunes with radii ranging from $1.94R_{\oplus}$ to $2.85R_{\oplus}$. Three of the planets have measured masses, yielding low bulk densities that suggest the presence of large hydrogen-dominated atmospheres.

HD 110067 (TIC 347332255) is a bright K0-type star in the constellation of Coma Berenices with mass and radius of approximately 80% of the Sun's. The Transiting Exoplanet Survey Satellite (TESS) monitored HD 110067 as part of its observations of Sector 23 (ref. 4). The data, processed by the TESS Science Processing Operations Center (SPOC)[5], exhibited several dips that could be associated with transiting planets. The SPOC reported two candidates: one with an orbital period of 5.642 days based on three dips with apparently similar depth and duration, and a second with an unconstrained orbital period based on a single event. The TESS reobserved the star 2 years later in Sector 49, revealing nine further transits incompatible with the previously announced candidates (Fig. 1).

Combining TESS Sectors 23 and 49, we could associate a fraction of the transits with two new planet candidates: HD 110067 b, a planet with an orbital period of 9.114 days, and HD 110067 c, a planet with an orbital period of 13.673 days. For the remaining unidentified transit events (two in Sector 23 and four in Sector 49), we attempted to match them by modelling them individually using a purely shape-based transit model agnostic to the orbital period (Methods and Extended Data Fig. 1). Then we compared them in duration–depth space, allowing us to identify two 'duo transits' (planets seen to transit only once in each of the two widely separated sectors) and two single transits (solitary transit events seen only in Sector 49). Duo transits have orbital periods limited to a finite number of harmonics or aliases that are constrained at the short-period end by the extent of continuous photometry observed before/after transit and at the long end by the distance between transits. Targeted observations with the CHaracterising ExOPlanets Satellite (CHEOPS)[6] allowed us to rule out many of these aliases and confirm a third planet in the system, HD 110067 d, with an orbital period of 20.519 days (Fig. 1).

The orbital periods of planets HD 110067 b, c and d (9.114, 13.673 and 20.519 days, respectively) have ratios very close to 3/2 ($P_c/P_b = 1.5003$ and $P_d/P_c = 1.5007$). Mean-motion resonances (MMRs) are orbital configurations in which the period ratio of a pair of planets is oscillating near a rational number of the form $(k + q)/k$, in which k and q are integers. First-order MMRs (in which $q = 1$) are the most common among planetary systems, as well as resonant chains. For the two innermost pairs of planets (bc and cd), we define two resonant angles $\phi_1 = 2\lambda_b - 3\lambda_c + \varpi_c$ and $\phi_2 = 2\lambda_c - 3\lambda_d + \varpi_c$, in which λ is the mean longitude of the planets and ϖ its longitude of periastron. Because $d\lambda_x/dt = 2\pi/P_x$, and given the aforementioned period ratios between b, c and d, a generalized Laplace relation links the triplet of planets through $2/P_b - 5/P_c + 3/P_d \approx 0$ (refs. 7–9). This relation ensures that the associated Laplace angle $\Psi_{bcd} = \phi_1 - \phi_2 = 2\lambda_b - 5\lambda_c + 3\lambda_d$ evolves slowly ($d\Psi_{bcd}/dt \approx 0$), indicating that the three planets might indeed be trapped in a Laplace chain of 3/2 resonances.

We explored the possibility that the remaining 'unmatched' dips correspond to planets that continue the first-order generalized Laplace resonant chain of HD 110067 b, c and d. Using a Laplace relation similar to that above, we can predict the possible orbital period of the planets, in a similar fashion to the discoveries of TOI-178 f and TRAPPIST-1 h (refs. 10,11). We assume that the next planet in the system must continue the generalized Laplace chain of first-order resonances. Considering the most common first-order MMRs (2/1, 3/2, 4/3, 5/4, 6/5), the only continuation of the chain that matches the spare duo transit supports the presence of a fourth planet in the system, HD 110067 e, with an orbital period of 30.7931 days (in a 3/2 MMR with planet d).

We are then left with two mono transits in TESS Sector 49, which we assume to correspond to two separate planets f and g that continue the chain. With single transits, we cannot use the same method as above and must introduce a new argument. In nature, all known three-body resonant chains are close to an equilibrium, that is, an equilibrium value of their angles Ψ (refs. 10,12–14) (Extended Data Fig. 2). Assuming low eccentricities, only the period and a single transit of each planet are required to estimate the value of Ψ. We can therefore try out different periods for planets f and g, then use their single transits to estimate Ψ_{def} and Ψ_{efg} and see if it lands close to an equilibrium of the chain. Here we

A list of authors and their affiliations appears at the end of the paper.

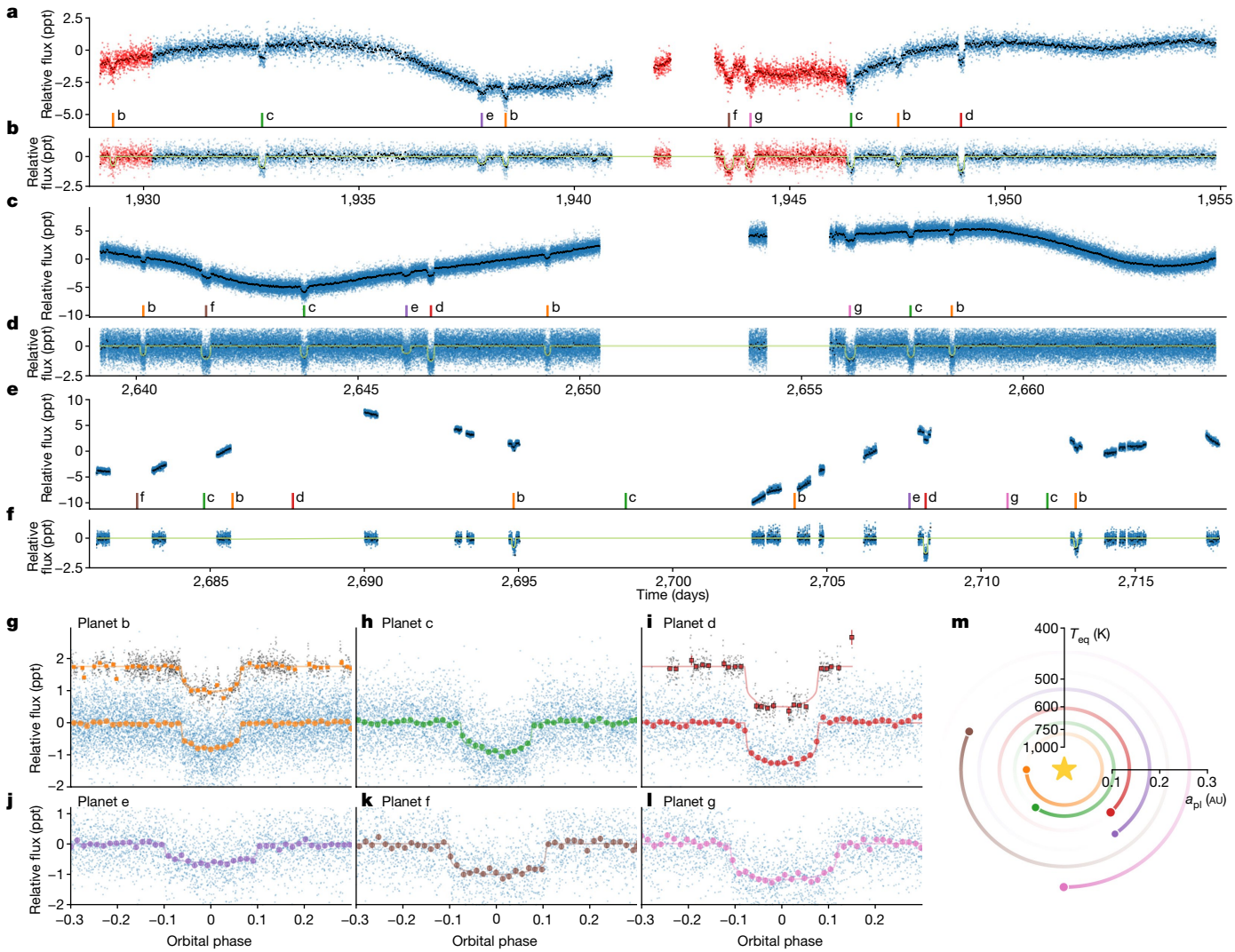

Fig. 1 | Space-based photometry from the TESS and the CHEOPS of HD 110067. Transits identified for each planet after our analyses are each associated with a different colour. **a**–**f**, Photometric time series of TESS Sector 23 (**a**,**b**, 2-min cadence), TESS Sector 49 (**c**,**d**, 20-s cadence) and CHEOPS (**e**,**f**). Red points in **a** show the reprocessed data affected by scattered light and high levels of sky background. Time units are in TESS Julian Date (TJD ≡ BJD − 2457000), in which BJD is the Barycentric Julian Date in units of days. Detrended light curves and the final model are shown in **b**,**d**,**f**. **g**–**l**, TESS phase-folded transits of each planet in the system. The transit model and binned photometry are colour-coded following the same convention. For HD 110067 b (**g**) and d (**i**), CHEOPS photometry is shown atop the TESS photometry with an arbitrary offset for clarity. **m**, Top-down view of the planetary system. Axes show the distance from the central star as a function of the semimajor axis and equilibrium temperature of the planet.

try the same set of first-order MMRs (2/1, 3/2, 4/3, 5/4, 6/5) between e and f and between f and g (50 combinations in total; see Methods). Of those, the only combination not excluded by existing data that can be close to an equilibrium of the chain is that in which $P_f/P_e = 4/3$ and $P_g/P_f = 4/3$, yielding the three outer generalized Laplace angles at less than 20° from the closest equilibrium (Methods, Extended Data Table 4 and Extended Data Fig. 3).

According to this prediction, planets HD 110067 f and g would have orbital periods of 41.0575 and 54.7433 days, respectively. If so, both planets would have transited during TESS Sector 23 observations, but during a time when the effect of scattered light and the relative contributions of the Earth and Moon to the image backgrounds were highly relevant. These frames are typically discarded, but a detailed reprocessing of the TESS Sector 23 observations triggered by this prediction showed two further transit events at 1943.6 TJD (TESS Julian Date, TJD ≡ BJD − 2457000) and 1944.1 TJD, matching exactly our model based on the resonant dynamics of the system (Fig. 1). Furthermore, a ground-based multi-instrument photometric campaign to catch a predicted transit of HD 110067 f (Methods and Extended Data Fig. 4) recovered a statistically significant detection (ΔWAIC = 9.5, in which WAIC is the Watanabe–Akaike information criterion) with a consistent depth and duration at the expected time, confirming its orbital period.

Also, we collected high-precision radial velocities of the star with the CARMENES (ref. 15) and HARPS-N (ref. 16) instruments. The dominant signals in the data correspond to the magnetic activity of the star rather than the planetary companions but, by applying state-of-the-art analyses to model stellar activity (Methods), we could independently confirm the detection of HD 110067 f, measuring an orbital period and phase (using agnostic priors on both quantities) that matched the transits. We used the radial velocities of the system to measure precise masses for three of the planets (HD 110067 b, d and f) and place upper limits on the remaining ones (Fig. 2). Although transit timing variations caused by the mutual gravitational interactions of the planets are expected in resonant systems[17], our photometric analysis did not measure any substantial deviation from the linear ephemeris (below 5 min for the inner triplet), probably because of the low number of individual transits

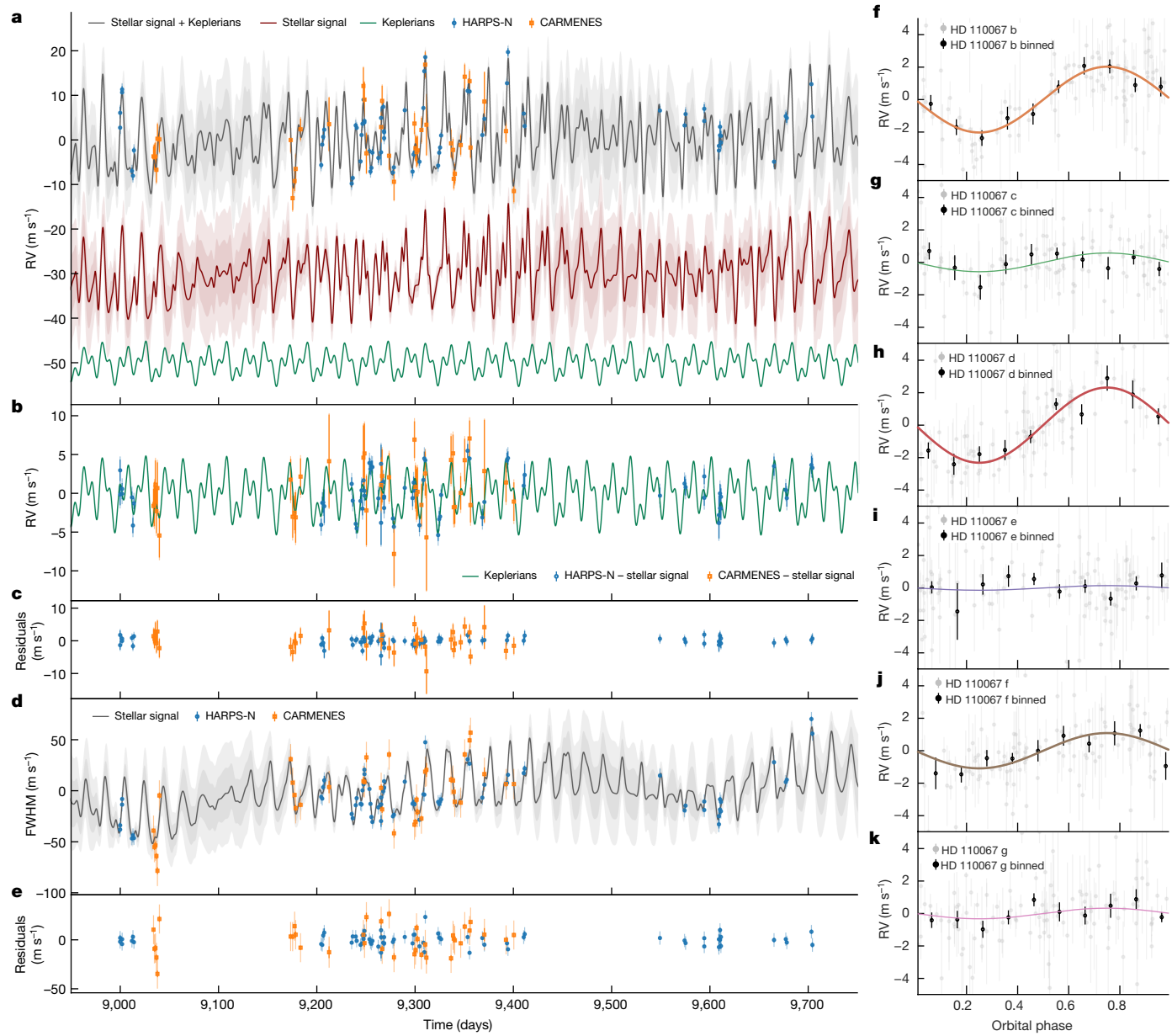

Fig. 2 | Radial velocity data from CARMENES and HARPS-N of HD 110067. Time units are the same as Fig. 1. **a**–**e**, Radial velocity (RV) and full-width at half-maximum (FWHM) time series after being corrected by inferred offsets. Each panel shows: RV data together with full, stellar and planetary inferred models (**a**); RV data with the stellar model subtracted (**b**); RV residuals (**c**); FWHM data together with the inferred stellar model (**d**); and FWHM residuals (**e**). HARPS-N (blue) and CARMENES (orange) measurements are shown by solid points with 1σ error bars, with a semitransparent error bar extension accounting for the inferred jitter. The solid lines show the inferred full model coming from our multidimensional Gaussian process model (Methods) and the lightly shaded areas show the 1σ and 2σ credibility intervals of the corresponding model. For the RV time series in **a**, we also show the inferred stellar (red) and planetary (green) recovered signals with an offset for clarity. **f**–**k**, Phase-folded RV signals for all the planets following the subtraction of the systemic velocities, stellar signal and other planets. Nominal RV observations are shown as light-grey points. Solid points show data binned to a tenth of the orbital phase. The inferred model is shown with a solid line following the colour-coding of Fig. 1. The planets with mass-measurement uncertainties smaller than 3σ (**f**,**h**,**j**) are marked with thicker lines.

for each planet. Further monitoring of the system will enable an independent measurement of the planetary masses using this technique.

The HD 110067 planetary system thus comprises at least six transiting planets orbiting in a chain of first-order MMRs (3/2–3/2–3/2–4/3–4/3). The planets have radii ranging between 1.94 and 2.85 times the radius of the Earth, orbital periods between 9 and 55 days and equilibrium temperatures between 440 and 800 K (Fig. 3). Thanks to the constraints on the planetary masses and their location above the radius valley[18,19], our internal composition modelling concludes that all the planets in the system (with the exception perhaps of planet e, which remains undetected in the radial velocity data) must have large hydrogen-dominated atmospheres to explain their relatively low bulk densities (see Supplementary Information). A summary of the most relevant properties of the system is presented in Table 1. We note that for both planets e and g, their orbital period measurement relies on a prediction based on the dynamical properties of the system, but an independent third transit observation confirming each orbit has not yet been obtained. Given the low mutual inclination of the system (less than 1°), further transiting planets may yet be found at periods longer than 70 days, which would correspond to orbits within or beyond the habitable zone of the star[20,21].

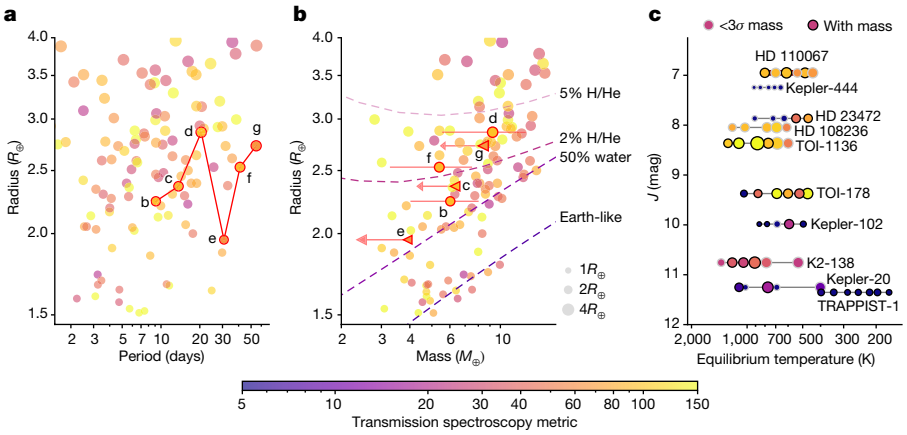

Fig. 3 | Properties of the HD 110067 system compared with the known sub-Neptune-sized planet population. a, Period–radius diagram. **b**, Mass–radius diagram. Mass–radius relationships for different planet compositions are taken from ref. 24. The 3σ mass upper limits are shown for planets HD 110067 c, e and g, with 1σ error bars for the rest. **c**, Host-star brightness in *J*-band magnitude as a function of planet equilibrium temperature showing systems with five or more transiting planets. Lower magnitudes indicate brighter stars. In all plots, point size is proportional to the planet radius, whereas the colour represents a proxy of the expected atmospheric scale height in transmission spectroscopy using the JWST following the metric of ref. 25. When mass is not known, we use the empirical mass–radius relation of ref. 26 to compute this metric. Planet population properties were retrieved from the NASA Exoplanet Archive on May 2023.

Table 1 | Summary of the planetary parameters of the HD 110067 system

Parameter[a]	HD 110067 b	HD 110067 c	HD 110067 d
Fit parameters			
P (days)	$9.113678 \pm 1 \times 10^{-5}$	$13.673694 \pm 2.4 \times 10^{-5}$	$20.519617 \pm 4 \times 10^{-5}$
t_0[b] (days)	2,640.15797±0.00036	2,657.45704±0.0007	2,708.20282±0.0008
$R_p/R_\star$	0.0256±0.0002	0.0278±0.0003	0.0332±0.0003
$b=(a/R_\star)\cos i_p$	0.355±0.033	0.155±0.078	0.488±0.023
$a/R_\star$	21.66±0.24	28.37±0.30	37.21±0.40
K (m s^{-1})	$2.03^{+0.62}_{-0.65}$	<1.55	$2.32^{+0.89}_{-0.88}$
Derived physical parameters			
M_p ($M_\oplus$)	$5.69^{+1.78}_{-1.82}$	<6.3	$8.52^{+3.31}_{-3.25}$
R_p ($R_\oplus$)	2.200±0.030	2.388±0.036	2.852±0.039
a_p (AU)	0.0793±0.00096	0.1039±0.0013	0.1362±0.0017
T_{eq} (K)[c]	800±10	699±9	602±8
t_T (days)[d]	0.12895±0.00078	0.15435±0.00121	0.15907±0.00158
i (°)	89.061±0.099	89.687±0.163	89.248±0.046
	†HD 110067 e	HD 110067 f	†HD 110067 g
Derived fit parameters			
P (days)	$30.793091 \pm 1.2 \times 10^{-5}$	$41.05854 \pm 1 \times 10^{-4}$	$54.76992 \pm 2 \times 10^{-4}$
t_0 (days)	2,646.0919±0.0011	2,641.5763±0.001	2,656.0921±0.002
$R_p/R_\star$	0.0226±0.0004	0.03026±0.00039	0.0303±0.00051
$b=(a/R\star)\cos i_p$	0.113±0.074	0.337±0.043	0.338±0.087
$a/R_\star$	48.77±0.52	59.08±0.52	71.59±0.78
K (m s^{-1})	<0.80	$1.09^{+0.40}_{-0.42}$	<1.30
Derived physical parameters			
M_p ($M_\oplus$)	<3.9	$5.04^{+1.89}_{-1.94}$	<8.4
R_p ($R_\oplus$)	1.940±0.040	2.601±0.042	2.607±0.052
a_p (AU)	0.1785±0.0022	0.2163±0.0026	0.2621±0.0032
T_{eq} (K)	533±7	489±6	440±6
t_T (days)	0.20265±0.00244	0.2152±0.0022	0.2361±0.0052
i (°)	89.867±0.089	89.673±0.046	89.729±0.073

[a]Error ranges denote the 68% posterior credibility intervals. Upper limits correspond to 99.7% posterior credibility intervals. [b]Mid-transit epoch is measured using the full baseline of transits observed with the TESS, the CHEOPS and ground-based facilities. Units are expressed in terms of the TESS Julian Date, TJD = BJD − 2457000, in which BJD is the Barycentric Julian Date in units of days. Reference time system is TDB (Barycentric Dynamical Time). [c]Equilibrium temperatures were calculated assuming zero Bond albedo and perfect energy redistribution. [d]Transit duration t_T is measured from the first to the last contact.

†The orbital period for planets e and g have been measured from their assigned duo transits placing a prior based on our prediction from the resonant chain analysis.

From an observational point of view, HD 110067 is the brightest star found to host more than four transiting exoplanets. The current delicate configuration of the planetary orbits in HD 110067 rules out any violent event over the billion-year history of the system[22], making it a rare 'fossil'[23] to study migration mechanisms and the properties of its protoplanetary disk in a pristine environment. The combination of host-star brightness and the inferred presence of extended atmospheres in most of its planets makes HD 110067 the most favourable multiplanetary sub-Neptune system to be observed in transmission spectroscopy with the James Webb Space Telescope (JWST) (Fig. 3). HD 110067 offers a chance to gain insight into the nature of sub-Neptune planets and where, how and under what conditions resonant chains form and survive.

Online content

Any methods, additional references, Nature Portfolio reporting summaries, source data, extended data, supplementary information, acknowledgements, peer review information; details of author contributions and competing interests; and statements of data and code availability are available at https://doi.org/10.1038/s41586-023-06692-3.

1. Howard, A. W. et al. Planet occurrence within 0.25 AU of solar-type stars from Kepler. *Astrophys. J. Suppl.* **201**, 15 (2012).
2. Fressin, F. et al. The false positive rate of Kepler and the occurrence of planets. *Astrophys. J.* **766**, 81 (2013).
3. Bean, J. L., Raymond, S. N. & Owen, J. E. The nature and origins of sub-Neptune size planets. *J. Geophys. Res. Planets* **126**, e06639 (2021).
4. Ricker, G. R. et al. Transiting Exoplanet Survey Satellite (TESS). *J. Astron. Telesc. Instrum. Syst.* **1**, 014003 (2015).
5. Jenkins, J. M. et al. in *Software and Cyberinfrastructure for Astronomy IV* (eds Chiozzi, G. & Guzman, J. C.) 99133E (SPIE, 2016).
6. Benz, W. et al. The CHEOPS mission. *Exp. Astron.* **51**, 109–151 (2021).
7. Sinclair, A. T. The orbital resonance amongst the Galilean satellites of Jupiter. *Mon. Not. R. Astron. Soc.* **171**, 59–72 (1975).
8. Morbidelli, A. *Modern Celestial Mechanics: Aspects of Solar System Dynamics* (Taylor & Francis, 2002).
9. Papaloizou, J. C. B. Three body resonances in close orbiting planetary systems: tidal dissipation and orbital evolution. *Int. J. Astrobiol.* **14**, 291–304 (2015).
10. Leleu, A. et al. Six transiting planets and a chain of Laplace resonances in TOI-178. *Astron. Astrophys.* **649**, A26 (2021).
11. Luger, R. et al. A seven-planet resonant chain in TRAPPIST-1. *Nat. Astron.* **1**, 0129 (2017).
12. Goździewski, K., Migaszewski, C., Panichi, F. & Szuszkiewicz, E. The Laplace resonance in the Kepler-60 planetary system. *Mon. Not. R. Astron. Soc.* **455**, L104–L108 (2016).
13. Agol, E. et al. Refining the transit-timing and photometric analysis of TRAPPIST-1: masses, radii, densities, dynamics, and ephemerides. *Planet Sci. J.* **2**, 1 (2021).
14. Dai, F. et al. TOI-1136 is a young, coplanar, aligned planetary system in a pristine resonant chain. *Astron. J.* **165**, 33 (2023).
15. Quirrenbach, A. et al. in *Ground-based and Airborne Instrumentation for Astronomy VIII*, (eds Evans, C. J., Bryant, J. J. & Motohara, K.) 114473C (SPIE, 2020).
16. Cosentino, R. et al. in *Ground-based and Airborne Instrumentation for Astronomy IV* (eds McLean, I. S., Ramsay, S. K. & Takami, H.) 84461V (SPIE, 2012).
17. Holman, M. J. & Murray, N. W. The use of transit timing to detect terrestrial-mass extrasolar planets. *Science* **307**, 1288–1291 (2005).
18. Fulton, B. J. et al. The California-Kepler survey. III. A gap in the radius distribution of small planets. *Astron. J.* **154**, 109 (2017).
19. Van Eylen, V. et al. An asteroseismic view of the radius valley: stripped cores, not born rocky. *Mon. Not. R. Astron. Soc.* **479**, 4786–4795 (2018).
20. Kasting, J. F., Whitmire, D. P. & Reynolds, R. T. Habitable zones around main sequence stars. *Icarus* **101**, 108–128 (1993).
21. Kopparapu, R. K. et al. Habitable zones around main-sequence stars: dependence on planetary mass. *Astrophys. J. Lett.* **787**, L29 (2014).
22. Izidoro, A. et al. Formation of planetary systems by pebble accretion and migration. Hot super-Earth systems from breaking compact resonant chains. *Astron. Astrophys.* **650**, A152 (2021).
23. Fabrycky, D. C. et al. Architecture of Kepler's multi-transiting systems. II. New investigations with twice as many candidates. *Astrophys. J.* **790**, 146 (2014).
24. Zeng, L. et al. Growth model interpretation of planet size distribution. *Proc. Natl Acad. Sci. USA* **116**, 9723–9728 (2019).
25. Kempton, E. M. R. et al. A framework for prioritizing the TESS planetary candidates most amenable to atmospheric characterization. *Proc. Acad. Sci. Pac.* **130**, 114401 (2018).
26. Otegi, J. F., Bouchy, F. & Helled, R. Revisited mass-radius relations for exoplanets below 120 $M_{\oplus}$. *Astron. Astrophys.* **634**, A43 (2020).

Publisher's note Springer Nature remains neutral with regard to jurisdictional claims in published maps and institutional affiliations.

Springer Nature or its licensor (e.g. a society or other partner) holds exclusive rights to this article under a publishing agreement with the author(s) or other rightsholder(s); author self-archiving of the accepted manuscript version of this article is solely governed by the terms of such publishing agreement and applicable law.

© The Author(s), under exclusive licence to Springer Nature Limited 2023

R. Luque[1]✉, H. P. Osborn[2,3,4,88], A. Leleu[2,5,88], E. Pallé[6,7,88], A. Bonfanti[8], O. Barragán[9], T. G. Wilson[10,11,12], C. Broeg[2,13], A. Collier Cameron[10], M. Lendl[5], P. F. L. Maxted[14], Y. Alibert[2,13], D. Gandolfi[15], J.-B. Delisle[5], M. J. Hooton[16], J. A. Egger[2], G. Nowak[6,7,17], M. Lafarga[11,12], D. Rapetti[18,19], J. D. Twicken[18,20], J. C. Morales[21,22], I. Carleo[6,23], J. Orell-Miquel[6,7], V. Adibekyan[24,25], R. Alonso[6,7], A. Alqasim[26], P. J. Amado[27], D. R. Anderson[11,12], G. Anglada-Escudé[21,22], T. Bandy[28], T. Bárczy[29], D. Barrado Navascues[30], S. C. C. Barros[31,32], W. Baumjohann[8], D. Bayliss[11], J. L. Bean[1], M. Beck[5], T. Beck[2], W. Benz[2,13], N. Billot[5], X. Bonfils[33], L. Borsato[34], A. W. Boyle[35], A. Brandeker[36], E. M. Bryant[11,26], J. Cabrera[37], S. Carrazco-Gaxiola[38,39,40], D. Charbonneau[41], S. Charnoz[42], D. R. Ciardi[35], W. D. Cochran[43,44], K. A. Collins[41], I. J. M. Crossfield[45], Sz. Csizmadia[37], P. E. Cubillos[8,23], F. Dai[35,46], M. B. Davies[47], H. J. Deeg[6,7], M. Deleuil[48], A. Deline[5], L. Delrez[49,50], O. D. S. Demangeon[31,32], B.-O. Demory[2,13], D. Ehrenreich[5,51], A. Erikson[37], E. Esparza-Borges[6,7], B. Falk[52], A. Fortier[2,13], L. Fossati[8], M. Fridlund[53,54], A. Fukui[6,55], J. Garcia-Mejia[41], S. Gill[11], M. Gillon[49], E. Goffo[15,56], Y. Gómez Maqueo Chew[38], M. Güdel[57], E. W. Guenther[56], M. N. Günther[28], A. P. Hatzes[56], Ch. Helling[8], K. M. Hesse[3,4], S. B. Howell[18], S. Hoyer[48], K. Ikuta[58], K. G. Isaak[28], J. M. Jenkins[18], T. Kagetani[58], L. L. Kiss[59,60], T. Kodama[55], J. Korth[61], K. W. F. Lam[37], J. Laskar[62], D. W. Latham[41], A. Lecavelier des Etangs[63], J. P. D. Leon[58], J. H. Livingston[64,65,66], D. Magrin[34], R. A. Matson[67], E. C. Matthews[68], C. Mordasini[2,13], M. Mori[58], M. Moyano[69], M. Munari[70], F. Murgas[6,7], N. Narita[6,55,64], V. Nascimbeni[34], G. Olofsson[36], H. L. M. Osborne[26], R. Ottensamer[57], I. Pagano[70], H. Parviainen[6,7], G. Peter[71], G. Piotto[34,72], D. Pollacco[11], D. Queloz[16,73], S. N. Quinn[41], A. Quirrenbach[74], R. Ragazzoni[34,72], N. Rando[28], F. Ratti[28], H. Rauer[37,75,76], S. Redfield[77,78], I. Ribas[21,22], G. R. Ricker[3,4], A. Rudat[3,4], L. Sabin[79], S. Salmon[5], N. C. Santos[31,32], G. Scandariato[70], N. Schanche[13,80], J. E. Schlieder[81], S. Seager[3,4,82,83], D. Ségransan[5], A. Shporer[3,4], A. E. Simon[2], A. M. S. Smith[37], S. G. Sousa[31], M. Stalport[50], Gy. M. Szabó[84,85], N. Thomas[2], A. Tuson[16], S. Udry[5], A. M. Vanderburg[3,4], V. Van Eylen[26], V. Van Grootel[50], J. Venturini[5], I. Walter[71], N. A. Walton[86], N. Watanabe[58], J. N. Winn[87] & T. Zingales[72]

[1]Department of Astronomy and Astrophysics, University of Chicago, Chicago, IL, USA. [2]Space Research and Planetary Sciences, Physics Institute, University of Bern, Bern, Switzerland. [3]Department of Physics, Massachusetts Institute of Technology, Cambridge, MA, USA. [4]Kavli Institute for Astrophysics and Space Research, Massachusetts Institute of Technology, Cambridge, MA, USA. [5]Observatoire Astronomique de l'Université de Genève, Versoix, Switzerland. [6]Instituto de Astrofisica de Canarias, La Laguna, Tenerife, Spain. [7]Departamento de Astrofisica, Universidad de La Laguna, La Laguna, Tenerife, Spain. [8]Space Research Institute, Austrian Academy of Sciences, Graz, Austria. [9]Sub-department of Astrophysics, Department of Physics, University of Oxford, Oxford, UK. [10]Centre for Exoplanet Science, SUPA School of Physics and Astronomy, University of St Andrews, St Andrews, UK. [11]Department of Physics, University of Warwick, Coventry, UK. [12]Centre for Exoplanets and Habitability, University of Warwick, Coventry, UK. [13]Center for Space and Habitability, University of Bern, Bern, Switzerland. [14]Astrophysics Group, Lennard Jones Building, Keele University, Keele, UK. [15]Dipartimento di Fisica, Universita degli Studi di Torino, Torino, Italy. [16]Cavendish Laboratory, University of Cambridge, Cambridge, UK. [17]Institute of Astronomy, Faculty of Physics, Astronomy and Informatics, Nicolaus Copernicus University, Toruń, Poland. [18]NASA Ames Research Center, Moffett Field, CA, USA. [19]Research Institute for Advanced Computer Science, Universities Space Research Association, Washington, DC, USA. [20]SETI Institute, Mountain View, CA, USA. [21]Institut de Ciencies de l'Espai (ICE-CSIC), Bellaterra, Spain. [22]Institut d'Estudis Espacials de Catalunya (IEEC), Barcelona, Spain. [23]INAF - Osservatorio Astrofisico di Torino, Pino Torinese, Italy. [24]Instituto de Astrofísica e Ciências do Espaço, Universidade do Porto, Porto, Portugal. [25]Departamento de Física e Astronomia, Faculdade de Ciências, Universidade do Porto, Porto, Portugal. [26]Mullard Space Science Laboratory, University College London, Dorking, UK. [27]Instituto de Astrofísica de Andalucía (IAA-CSIC), Granada, Spain. [28]European Space Research and Technology Centre (ESTEC), European Space Agency (ESA), Noordwijk, The Netherlands. [29]Admatis, Miskolc, Hungary. [30]Depto. de Astrofisica, Centro de Astrobiología (INTA-CSIC), Madrid, Spain. [31]Instituto de Astrofisica e Ciencias do Espaco, Universidade do Porto, Porto, Portugal. [32]Departamento de Fisica e Astronomia, Faculdade de Ciencias, Universidade do Porto, Porto, Portugal. [33]Université Grenoble Alpes, CNRS, IPAG, Grenoble, France. [34]INAF - Osservatorio Astronomico di Padova, Padova, Italy. [35]Department of Astronomy, California Institute of Technology, Pasadena, CA, USA. [36]Department of Astronomy, Stockholm University, AlbaNova University Center, Stockholm, Sweden. [37]Institute of Planetary Research, German Aerospace Center (DLR), Berlin, Germany. [38]Instituto de Astronomía, Universidad Nacional Autónoma de México, Ciudad de México, Mexico. [39]Department of Physics and Astronomy, Georgia State University, Atlanta, GA, USA. [40]RECONS Institute, Chambersburg, PA, USA. [41]Center for Astrophysics | Harvard & Smithsonian, Cambridge, MA, USA. [42]Université de Paris Cité, Institut de Physique du Globe de Paris, CNRS, Paris, France. [43]McDonald Observatory, The University of Texas, Austin, TX, USA. [44]Center for Planetary Systems Habitability, The University of Texas, Austin, TX, USA. [45]Department of Physics and Astronomy, University of Kansas, Lawrence, KS, USA. [46]Division of Geological and Planetary Sciences, California Institute of Technology, Pasadena, CA, USA. [47]Centre for Mathematical Sciences, Lund University, Lund, Sweden. [48]Aix Marseille Univ., CNRS, CNES, LAM, Marseille, France. [49]Astrobiology Research Unit, Université de Liège, Liège, Belgium. [50]Space sciences,

Technologies and Astrophysics Research (STAR) Institute, Université de Liège, Liège, Belgium. [51]Centre Vie dans l'Univers, Faculté des sciences, Université de Genève, Genève 4, Switzerland. [52]Space Telescope Science Institute, Baltimore, MD, USA. [53]Leiden Observatory, University of Leiden, Leiden, The Netherlands. [54]Onsala Space Observatory, Department of Space, Earth and Environment, Chalmers University of Technology, Onsala, Sweden. [55]Komaba Institute for Science, The University of Tokyo, Tokyo, Japan. [56]Thüringer Landessternwarte Tautenburg, Tautenburg, Germany. [57]Department of Astrophysics, University of Vienna, Vienna, Austria. [58]Department of Multi-Disciplinary Sciences, Graduate School of Arts and Sciences, The University of Tokyo, Tokyo, Japan. [59]Konkoly Observatory, HUN-REN Research Centre for Astronomy and Earth Sciences, Budapest, Hungary. [60]Institute of Physics, ELTE Eötvös Loránd University, Budapest, Hungary. [61]Lund Observatory, Division of Astrophysics, Department of Physics, Lund University, Lund, Sweden. [62]IMCCE, UMR8028 CNRS, Observatoire de Paris, PSL Univ., Sorbonne Univ., Paris, France. [63]Institut d'Astrophysique de Paris, UMR7095 CNRS, Université Pierre & Marie Curie, Paris, France. [64]Astrobiology Center, Tokyo, Japan. [65]National Astronomical Observatory of Japan, Tokyo, Japan. [66]Department of Astronomical Science, The Graduate University for Advanced Studies, SOKENDAI, Tokyo, Japan. [67]United States Naval Observatory, Washington, DC, USA. [68]Max Planck Institute for Astronomy, Heidelberg, Germany. [69]Instituto de Astronomía, Universidad Católica del Norte, Antofagasta, Chile. [70]INAF - Osservatorio Astrofisico di Catania, Catania, Italy. [71]Institute of Optical Sensor Systems, German Aerospace Center (DLR), Berlin, Germany. [72]Dipartimento di Fisica e Astronomia "Galileo Galilei", Universita degli Studi di Padova, Padova, Italy. [73]Department of Physics, ETH Zurich, Zurich, Switzerland. [74]Landessternwarte, Zentrum für Astronomie der Universität Heidelberg, Heidelberg, Germany. [75]Zentrum für Astronomie und Astrophysik, Technische Universität Berlin, Berlin, Germany. [76]Institut für Geologische Wissenschaften, Freie Universität Berlin, Berlin, Germany. [77]Astronomy Department, Wesleyan University, Middletown, CT, USA. [78]Van Vleck Observatory, Wesleyan University, Middletown, CT, USA. [79]Instituto de Astronomía, Universidad Nacional Autónoma de México, Ensenada, Mexico. [80]Department of Astronomy, University of Maryland, College Park, MD, USA. [81]NASA Goddard Space Flight Center, Greenbelt, MD, USA. [82]Department of Earth, Atmospheric and Planetary Sciences, Massachusetts Institute of Technology, Cambridge, MA, USA. [83]Department of Aeronautics and Astronautics, Massachusetts Institute of Technology, Cambridge, MA, USA. [84]Gothard Astrophysical Observatory, ELTE Eötvös Loránd University, Szombathely, Hungary. [85]HUN-REN-ELTE Exoplanet Research Group, Szombathely, Hungary. [86]Institute of Astronomy, University of Cambridge, Cambridge, UK. [87]Department of Astrophysical Sciences, Princeton University, Princeton, NJ, USA. [88]These authors contributed equally: H. P. Osborn, A. Leleu, E. Pallé. ✉e-mail: rluque@uchicago.edu

Methods

Data

TESS photometry. HD 110067 was observed in TESS Sectors 23 and 49 (18 March 2020 to 16 April 2020 and 26 February 2022 to 26 March 2022, respectively) (ref. 4). The star was included on the TESS Candidate Target List (CTL)[27] and therefore the target was observed at 120-s cadence in both sectors. The target images are processed by the TESS SPOC pipeline at NASA Ames[5], which calibrates the pixels, performs simple aperture photometry (SAP), flags poor-quality data and removes systematic trends to create the so-called 'Presearch Data Conditioning' light curve (PDCSAP)[28–30]. Finally, the SPOC pipeline runs a wavelet-based transiting planet search for periodic exoplanets[31–33], which—in the case of the Sector 23 data—revealed two threshold-crossing events (TCEs)—that is, candidate planets—which passed data validation checks[34,35]. Manual vetting of these two candidates resulted in the assignment of two TESS Objects of Interest (TOI), namely, TOI-1835.01 and TOI-1835.02 (ref. 36).

The first TCE was alerted by SPOC as TOI-1835.01 with a period of 5.641 days. Although two of the three transits associated with this ephemeris seemed to be of similar depth and duration, the third did not seem to be associated with a clear transit. However, this could have been because of the proximity to a systematic dip caused by a momentum dump. A second TCE, TOI-1835.02, was alerted as a single transit at 1948.98 TJD, as opposed to the period of 11.107 days proposed by the SPOC owing to an apparent discrepancy in the transit depth between the two transits purportedly linked by the transiting planet search. On the other hand, a peak in the background flux ruled out the planetary origin of an apparent transit feature at TJD = 1940.5. Both the depth and shape of this feature were strongly dependent on the detrending method used in the light curve, which is indicative of its spurious nature.

HD 110067 was later reobserved by TESS in Sector 49. To confirm the TCEs and plan immediate follow-up, we downloaded the TESS Image CAlibrator Full Frame Images (TICA FFI)[37] only a week after downlink for each of the first and then second orbits. We computed a light curve from the 10-min cadence TICA FFI cut-outs using SAP and clipped regions of high brightness because of the Earth and Moon, as well as parts of the light curve affected by systematics such as momentum dumps. The first orbit alone revealed at least five new clear-transit features. These all seemed to have varying depths and durations and none were compatible with the 5.64-day period implied by TOI-1835.01. The second orbit showed three more clear transit events, making a total of eight in Sector 49 and five in Sector 23. A 20-s cadence target pixel file was later made available for HD 110067, which resulted in higher-precision photometry.

Manual vetting of both Sectors 23 and 49 PDCSAP light curves revealed unexpectedly large systematic uncertainties (Gini's mean difference, that is, the average point-to-point absolute difference, of 215 ppm in 3-h bins) that were absent from the uncorrected SAP flux. This has been seen in many bright stars that have stellar variability (for example, refs. 38,39). To better correct these systematics, we performed a custom extraction of the TESS light curves for both sectors using the quaternion detrending technique against spacecraft motion developed in ref. 40. This involved fitting a model consisting of a linear combination of a basis spline (with breakpoints spaced every 1.5 days to model long-timescale stellar or instrumental variability) and decorrelation with parameters linked to systematic flux changes, namely, the means and standard deviations of the spacecraft quaternion time series (and the squared time series) within each exposure. Using a linear least squares technique (matrix inversion), we solved for the best-fit coefficients of our free parameters while iteratively excluding 3σ outliers from the fit until convergence was reached. After calculating the best-fit model for the systematics of each aperture, we then subtracted it from the uncorrected light curve and identified the aperture that produced the light curve with the lowest photometric scatter. The final light curves used in our subsequent analyses (Gini's mean difference of 130 ppm in 3-h bins) are shown in Fig. 1.

Finally, as discussed above, a large portion of the data was missing from the PDCSAP light curves because of high levels of scattered light and sky background from the Earth and Moon. The dates affected coincide with the potential transit events of planets f and g based on our dynamical model prediction. Therefore, to recover data affected by scattered light, we performed a custom extraction of the TESS light curves for both sectors using a pixel level decorrelation (PLD) method[41–43] implemented in the PLDCorrector class of the community Python package lightkurve (ref. 44). This method uses: (1) a spline polynomial fit to describe stellar variability; (2) principal component analysis (PCA) eigenmodes to model the background light; and (3) the PLD technique to account for pointing and mechanical effects. Before applying the PLDCorrector, we add the background flux and errors estimated by the TESS SPOC pipeline back onto the SAP light curve. Flux level, fraction and crowding adjustments are then applied to the corrected light curve. To automatically optimize the selection of parameter values for the PLDCorrector, we evaluate the resulting light curve using the Savitzky–Golay combined differential photometric precision (sgCDPP) proxy algorithm[45,46] implemented in lightkurve. For a grid of PLDCorrector parameter values, we calculate the harmonic mean of these quantities and select the corrected light curve that minimizes it. We use these data for the cadences missing in the quaternion-detrended light curve in our final analyses (marked with a different colour in Fig. 1).

CHEOPS photometry. The CHEOPS mission is a European Space Agency small-class mission dedicated to studying bright, nearby exoplanet host stars for the purpose of making high-precision photometric observations of transiting planets[6]. We collected 19 separate visits of HD 110067 with the CHEOPS between 11 April 2022 and 17 May 2022 under Guaranteed Time Observing programmes ID-048 and ID-031. The goal of these observations is (1) to confirm the true orbital period of single-transiting and duo-transiting planet candidates and (2) to improve the planetary radius precision and ephemeris of confirmed planets. This has been done for large planets producing deep eclipses from the ground[47,48] and for small planets from space[39,49,50]. An observing log summarizing the duration of each visit, its average observing efficiency (considering the gaps produced by Earth occultations or passages over the South Atlantic Anomaly along the low-Earth orbit of the spacecraft) and photometric precision are presented in Extended Data Table 1.

To provide the highest-quality photometric precision, we opted to perform custom photometric extraction of the CHEOPS imagettes using point-spread-function (PSF) photometry as implemented by the PIPE package[51,52]. For bright targets such as HD 110067, light curves generated with PIPE exhibit lower median absolute differences than those generated by the CHEOPS Data Reduction Pipeline[53]. The shorter cadence of the CHEOPS imagettes allows a higher cadence light curve and PSF detrending is also better at removing trends owing to systematic factors and background stars. As various PSF models have already been generated and vary as a function of stellar temperature, we opted to use a PSF generated using the star HD 189733, with a similar spectral type as HD 110067. To preserve inter-visit flux differences, we normalized the entire CHEOPS data together instead of individually. This revealed clear visit-to-visit flux differences owing to stellar rotation with an amplitude larger than that of the TESS (as stellar activity is typically more pronounced at bluer bandpasses). The final light curves used in our subsequent analyses are shown in Fig. 1 and Supplementary Fig. 1.

Ground-based photometric campaign. We carried out a campaign on the night of 23 May 2022 to attempt to confirm the 41.05-day period orbit of HD 110067 f as predicted by our resonance chain analysis. Photometric observations were taken using 14 telescopes

using seven different filters, which observed from various locations to continuously cover a temporal baseline of more than 11 h (between 22:52:55UT 23 May 2022 and 10:01:33UT 24 May 2022). This window is long enough to catch the 5-h transit expected from 02:52UT to 07:12UT. However, no single location was able to cover both ingress and egress. A summary of the observations is shown in Extended Data Table 2. Details from each individual observation are shown below. Extended Data Fig. 4 shows the data and best-fit models as discussed in the section 'Confirming the predictions'.

Teide Observatory. We observed HD 110067 on 23 May 2022 using the MuSCAT2 instrument installed at the 1.5-m Telescopio Carlos Sánchez (TCS) located at the Teide Observatory, Spain[54]. The images were taken simultaneously in g, r, i and z_s filters with the telescope heavily defocused and with short exposure times of 3–5 s, depending on the band, to avoid saturation. Relative light curves for each band and instrument of HD 110067 were extracted by aperture photometry using a custom pipeline[55] with optimal aperture radii of 8.1″ to 11.3″, depending on the band. Note that there was a technical problem on the dome of the TCS between BJD-2459723 = 0.488 and 0.526; we discarded the data taken during this period.

We also observed HD 110067 on 23 May 2022 with one of the 1-m telescopes from Las Cumbres Observatory (LCO) global network located at the Teide Observatory, Spain[56]. The observations were obtained through Director's Discretionary Time programme 2022A-005 (PI: Wilson). We collected 181 frames with an exposure time of 20 s, covering 2.5 h, using the 4,096 × 4,096-pixel SINISTRO camera. The images were calibrated by the standard LCO BANZAI pipeline[57]. Differential photometric data were extracted using AstroImageJ (AIJ)[58].

Paranal Observatory. We observed HD 110067 on 23 May 2022 using the Next-Generation Transit Survey (NGTS) facility located at the European Southern Observatory's (ESO) Paranal Observatory in Chile[59]. The NGTS consists of twelve 20-cm, f/2.8 telescopes with Andor cameras and red-sensitive (600–900 nm) deep-depletion e2v CCDs. Nine NGTS telescopes observed from 23:14UT to 04:35UT, covering a predicted transit ingress of HD 110067 f and spanning an air mass range of 1.7–2.5. Two telescopes started observing 2 h late owing to a technical issue. All nine telescopes were defocused to avoid saturating the bright target star during the 10-s exposures. The NGTS camera shutters were not functional and so were kept open during the entire observing block. That caused the stars to streak during the 1.5-s readout sequences but without any apparent detrimental effect on the photometry. Observing without using the shutters is now the standard operation mode of the NGTS. We performed standard differential aperture photometry, using large aperture radii of 6.5–8.0 pixels, and carefully selecting comparison stars to avoid those that exhibited variability. The light curve of each telescope was normalized individually and no detrending was performed.

F. L. Whipple Observatory. We observed HD 110067 on 24 May 2022 using the Tierras instrument installed at the refurbished 1.3-m telescope located at the F. L. Whipple Observatory atop Mount Hopkins, Arizona, USA. The instrument is designed to regularly achieve a photometric precision of 250 ppm on timescales of both 10 min and a complete observing season. The design choices that permit this precision include a four-lens focal reducer and field flattener that increase the field-of-view of the telescope, a custom narrow-bandpass filter centred around 863.5 nm to minimize precipitable water vapour errors and a fully automated mode of operation[60]. A total of 1,262 4-s exposures were gathered with Tierras for HD 110067. Astrometric calibrations were done in real time during data gathering and were stored in WCS headers in the FITS files. The FITS files were then passed through the Tierras image-reduction pipeline to perform bias corrections and image stitching (the CCD chip is read out through separate amplifiers). AIJ was used for photometric extraction. These observations were gathered shortly after Tierras started science operations and the data were not flat-fielded because knowledge of the flat field was incomplete at the time. The r.m.s. of the 15-min binned data is 323 ppm. The photometric precision on this target is ultimately limited by scintillation, as the target was observed down to an air mass of 2.37. The observations were mildly affected by cirrus.

San Pedro Mártir Observatory. We observed HD 110067 on 24 May 2022 with the 1-m SAINT-EX telescope at the Observatorio Astronómico Nacional de la Sierra de San Pedro Mártir in Baja California, Mexico[61]. SAINT-EX is equipped with a deep-depleted and back-illuminated Andor IKON CCD and a filter wheel. The observations were defocused and acquired in the 'zcut' filter, a custom filter optimized to reduce the systematic uncertainties in the light curves of red stars resulting from precipitable water vapour, with an exposure time of 10 s. The data were reduced with AIJ using the standard corrections for bias, flat-fielding and dark current. AIJ was also used to carry out the aperture photometry of the time series, producing the light curves and relevant metadata. The observations were mildly affected by high-altitude cirrus.

Haleakala Observatory. We observed HD 110067 on 24 May 2022 using the MuSCAT3 instrument mounted on the 2-m Faulkes Telescope North (FTN) at Haleakala Observatory on Maui, Hawaii, USA[62]. The images were taken simultaneously in g, r, i and z_s filters with the telescope heavily defocused and with short exposure times of 3–5 s, depending on the band, to avoid saturation. Relative light curves for each band and instrument were extracted by aperture photometry using a custom pipeline[63] with optimal aperture radii of 8.1″ to 11.3″, depending on the band. There was a guiding issue on the FTN around BJD-2459723 = 0.795, which caused a large shift of the stellar positions on the detectors; we treated the MuSCAT3 data as two independent datasets separated by that time.

High-resolution imaging. As part of our standard process for validating transiting exoplanets, and to assess the possible contamination of bound or unbound companions on the derived planetary radii[64], we observed HD 110067 with near-infrared adaptive optics (AO) imaging at Palomar Observatory and with optical speckle imaging at Gemini North. Gaia DR3 is also used to provide further constraints on the presence of undetected stellar companions and wide companions. No close-in ($\lesssim$1″) stellar companions were detected by either the near-infrared AO or optical speckle imaging.

Palomar Observatory. The Palomar Observatory observations of HD 110067 were made with the PHARO instrument[65] behind the natural guide star AO system P3K (ref. 66) on 8 January 2020 in a standard five-point quincunx dither pattern with steps of 5″ in the narrow-band Br-γ filter. Each dither position was observed three times, offset in position from each other by 0.5″ for a total of 15 frames, with an integration time of 1.4 s per frame for total on-source times of 21 s. PHARO has a pixel scale of 0.025″ per pixel for a total field of view of approximately 25″. The sensitivities of the final combined AO image were determined by injecting simulated sources azimuthally around the primary target every 20° at separations of integer multiples of the central source's full width at half maximum (FWHM)[67]. The Palomar data have a sensitivity Δmag = 2 at 0.1″ and Δmag = 9 at 1″; the final sensitivity curve is shown in Supplementary Fig. 2.

Gemini Observatory. We observed HD 110067 with the Alopeke speckle imaging camera at Gemini North on 10 June 2020 (ref. 68). We obtained five sets of 1,000 frames, each frame having an integration time of 60 ms, obtaining images in each of the instrument's two bands (centred at 562 nm and 832 nm). The observations were reduced using our standard software pipeline[69] and reached a 5σ sensitivity of Δmag = 7 (blue channel) and Δmag = 6.8 (red channel) at separations of 0.5″. The reconstructed speckle images show no evidence of other nearby point sources. The final sensitivity curve is shown in Supplementary Fig. 2.

Gaia Space Observatory. As well as the high-resolution imaging, we have used Gaia to identify any wide stellar companions that may be bound members of the system[70,71]. There are no further widely separated companions identified by Gaia that have the same distance and proper

motion as HD 110067. Furthermore, the Gaia DR3 astrometry provides extra information on the possibility of inner companions that may have gone undetected by either Gaia or the high-resolution imaging data. The Gaia renormalized unit weight error (RUWE) is a metric, similar to a reduced chi-square, in which values that are $\lesssim$1.4 indicate that the Gaia astrometric solution is consistent with the star being single, whereas RUWE values $\gtrsim$1.4 may indicate an astrometric excess noise, possibly caused by the presence of an unseen companion (for example, ref. 72). HD 110067 has a Gaia EDR3 RUWE value of 0.94, indicating that the astrometric fit is consistent with a single-star model.

Radial velocity monitoring. Calar Alto Observatory. We observed HD 110067 using the CARMENES instrument[15] installed at the 3.5-m telescope of Calar Alto Observatory in Almería, Spain, between 3 July 2020 and 4 July 2021. We collected 39 high-resolution spectra under the observing programmes F20-3.5-011 (PI: Nowak) and H20-3.5-013 (PI: Luque). Radial velocities and further spectral indicators were derived using raccoon (ref. 73) and serval (ref. 74). Although the mean internal precision of the template-matching serval radial velocities is 3.1 m s^{-1}, the precision of the cross-correlation method raccoon radial velocities is 2.9 m s^{-1}, so we used the latter in our analyses.

Roque de los Muchachos Observatory. We observed HD 110067 with the HARPS-N spectrograph mounted at the 3.6-m Telescopio Nazionale Galileo[16] of Roque de los Muchachos observatory in La Palma, Spain, between 30 May 2020 and 4 May 2022. We collected 72 high-resolution spectra under the observing programmes CAT19A_162 (PI: Nowak), CAT21A_119 (PI: Nowak) and ITP19_1 (PI: Pallé) that were used to measure the photospheric properties of the star and precise radial velocities. Radial velocities and further spectral indicators were derived using an online version of the DRS pipeline[75], the YABI tool and serval[74]. Both the YABI-derived and serval-derived radial velocities have a median internal precision of 1.0 m s^{-1}, but we used the YABI ones (based on the cross-correlation method) in our final analyses for consistency with the CARMENES dataset.

Stellar parameters

Photospheric parameters and abundances. To properly characterize the planetary system around HD 110067, we first conduct a series of analyses to determine the properties of the host star. We derive the stellar spectral parameters by applying the widely used ARES+MOOG tools to our co-added HARPS-N spectra[76–78]. ARES (refs. 79,80) measures the equivalent widths of iron lines in the spectrum that are converted into stellar atmospheric parameters using the MOOG radiative transfer code[81] applied to Kurucz model atmospheres[82]. In Extended Data Table 3, we report the effective temperature $T_{\rm eff}$, surface gravity $\log g$ and metallicity [Fe/H] obtained on convergence of ionization and excitation equilibria using this method. Furthermore, we measure the stellar $v\sin i$ from the HARPS-N spectra using ZASPE (ref. 83).

We further study the photospheric parameters by conducting a classical curve-of-growth analysis on our co-added HARPS-N spectrum using our aforementioned spectral parameters to obtain [Mg/H] and [Si/H] abundances for HD 110067. Using the ARES+MOOG framework detailed above, we obtain the equivalent widths[80] for these elements, which are converted to abundances assuming local thermodynamic equilibrium[81,82]. The specific details of this analysis are beyond the scope of this paper and can be found in refs. 84,85. We report the stellar abundances in Extended Data Table 3.

Physical parameters. Using our spectral parameters and the ATLAS[82,86] and PHOENIX[87] catalogues, we build spectral energy distributions of HD 110067 that we compare to optical and infrared broadband photometry of the star (see Extended Data Table 3) to derive the stellar angular diameter and effective temperature by means of the infrared flux method[88]. This is conducted in a Markov chain Monte Carlo (MCMC) approach[89,90], with which we convert the angular diameter to the stellar radius using the Gaia EDR3 offset-corrected parallax[91] with model uncertainties accounted for using a Bayesian modelling averaging. We report the stellar radius $R_\star$ in Extended Data Table 3.

Last, we complete our stellar characterization by determining the mass and age of HD 110067. We constrain two sets of stellar evolutionary models with the help of our derived values for $T_{\rm eff}$, $\log g$ and $R_\star$ (ref. 92). On the one hand, we use an isochrone placement algorithm[93,94] and interpolate over precomputed grids of PARSEC v1.2s (ref. 95) isochrones. On the other hand, we use the Code Liègeois d'Évolution Stellaire (CLES)[96] combined with a Levenberg–Marquardt minimization scheme[97] to optimize the best-fitting evolutionary track. The results from the two methods are combined to determine the mass and age of the star that is reported in Extended Data Table 3.

The [Fe/H] and age of HD 110067 indicate that this star could belong to the galactic thick disk stellar population or be an older member of the galactic thin disk. The values of [Mg/H] and [Si/H], being within 1σ of [Fe/H], show that the star is not enhanced in α-capture elements and are indicative of a typical thin disk chemical composition. We determined the kinematic properties of HD 110067 by using the Gaia EDR3 astrometry to compute the local standard of rest space velocities of this star following ref. 98. From these velocities, we compute that the probability of kinematic membership in the galactic thin disk is 0.9911 ± 0.0029. Thus, we conclude that HD 110067 is on the older, more metal-poor end of the distribution of the galactic thin disk stellar population.

Analysis

Space-based photometry modelling. We performed simultaneous modelling of the space-based photometry. We used the quaternion-detrended TESS data combined with the PLD-detrended data for the missing Sector 23 gaps and the PIPE-detrended CHEOPS data for the three visits containing transits. We built transit models for the six planets with exoplanet (ref. 99). Owing to its nature as a rotating telescope on a near-Earth orbit, even PSF-detrended CHEOPS photometry can include systematic trends. However, these typically correlate with other measurements, for example, roll angle, background or contaminant flux. To not bias the transit model and to better propagate uncertainties on the derived parameters, we performed CHEOPS decorrelation alongside our photometric transit modelling. We first fitted each CHEOPS transit individually alongside several possible decorrelation factors, allowing us to assess which decorrelation factors are most useful. This also enabled us to test whether such decorrelation is shared among all CHEOPS visits or individual to a single light curve. From this analysis, we included the following parameters in the linear correlation: position centroids, the second harmonic of the cosine of the roll angle, $\cos 2\Phi$, the change in telescope temperature and quadratic trends with the x–y centroids. CHEOPS data have also been known to contain flux trends that vary stochastically as a function of roll angle over shorter frequencies (see, for example, ref. 100). These are not well removed using simple trigonometric functions, hence we also modelled a flexible spline shared between all visits to model shorter-timescale variation. To incorporate stellar variability, a floating mean and flux trend were also fitted to each CHEOPS visit, as well as an individual jitter term.

Informative priors were used on limb-darkening parameters using the theoretical quadratic limb-darkening parameters for TESS (ref. 101) and CHEOPS (ref. 102), with uncertainties inflated to 0.1 in all cases to guard against systematic offsets. The impact parameter and radius ratio are fitted from a broad uniform and log-normal prior, respectively, whereas the period and mid-transit epoch are fitted using broad normal priors from the transits identified and modelled above. Stellar parameters from Extended Data Table 3 were used as inputs to the model with Gaussian priors. Orbits were assumed to be circular in all cases, which is a good approximation for planetary systems with several transiting planets[103–105]. The prior and posterior distributions of each parameter in the model are shown in Supplementary Table 1.

Properties of the unmatched transits. Our first modelling of the TESS space-based photometry was able to account for a total of five transits of planet b (two in TESS Sector 23 and three in TESS Sector 49) and four transits of planet c (two each in TESS Sectors 23 and 49). However, this analysis left six 'unmatched' transits in the original TESS light curves. To pair the transits, we fitted each transit individually using a purely shape-based transit model agnostic to the orbital period using MonoTools[106]. From this analysis, we then compared each transit in duration–depth space, allowing us to clearly see that both transits from Sector 23 shared unique regions of this parameter space with two more transits seen in Sector 49 (duo transits), whereas the two longest-duration transits seen only in Sector 49 were solitary (mono transits). Extended Data Fig. 1 shows this result.

We then modelled both duo transits and single transits using MonoTools fitting. This allows long-period planets to be modelled in a way that the transit model is agnostic of the orbital period with the implied period distributions being manipulated using priors. This technique works for single transits or duo transits. In the case of two transit events separated by a long gap, the planetary transit is fitted leaving the orbital period open and the implied transit shape is used to calculate the probability for each of the possible period aliases. For single transits, potential orbital period windows are computed. In both cases, the period probability distribution comes from a combination of a simple period prior (longer-period planets are geometrically disfavoured)[107], an eccentricity prior (eccentric orbits are disfavoured in multitransiting systems)[108] and a stability prior using the orbits of other planets in the system (orbit-crossing is disallowed) (further details in refs. 39,109). The resulting marginalized period predictions for planets HD 110067 d, e, f and g are shown in Supplementary Fig. 3, with posterior values of $21.6^{+2.9}_{-1.6}$, $29.9^{+4.6}_{-3.3}$, $40.1^{+7.1}_{-5.1}$ and 47.0 ± 8.0 days, respectively.

Continuing the resonant chain. In this section, we expand the analyses that led to the prediction of the orbits of planets HD 110067 e, f, and g based on the generalized Laplace resonant configuration of the three inner transiting planets in the system. We assume that all events mentioned in the previous section are transits that belong to planets that continue the resonant chain.

For transiting systems, generalized three-body Laplace angles can be estimated in the zeroth order in eccentricity, defined as $\Psi_{e=0}$, from the times of mid-transit and the orbital period of the planets (see, for example, ref. 110). This estimation differs from the actual generalized three-body Laplace angle proportionally to the eccentricities (equation (15) of ref. 111). Notably, for known systems with a chain of three-body resonances, all $\Psi_{e=0}$ lie close to an equilibrium of the chain, as seen in Extended Data Fig. 2. The largest distance is about 43° for the inner triplet of K2-138 (ref. 112). For HD 110067, the estimated angle $\Psi_{e=0,\mathrm{bcd}}$ is also at about 44° from its theorized 180° equilibrium. Through the study of transit timing variations over several years, we can obtain constraints on the underlying generalized three-body Laplace angles. In known cases, we can see that these angles oscillate with amplitudes of a few tens of degrees at most around their equilibrium value (see Fig. 2 of ref. 12 for Kepler-60 and Fig. 25 of ref. 13 for TRAPPIST-1).

As shown above, the two events at 2646.088 TJD and 1937.851 TJD have fully consistent shapes. Among the probable periods computed with MonoTools (Supplementary Fig. 3), P_e = 30.7931 days is the only one that continues the resonant chain, with P_e/P_d = 1.5007, landing inside the common 3:2 MMR (see Supplementary Fig. 4). We compute the observed value of the associated generalized three-body Laplace angle $\Psi_{e=0,\mathrm{cde}}$ = 169.995°, which is at only 10° from the expected 180° equilibrium. We hence predict a period of 30.7931 days for planet HD 110067 e if it is in the resonant chain.

For the remaining two mono transits, we try a set of first-order MMRs (2/1, 3/2, 4/3, 5/4, 6/5) between planets 4 and 5 and the same between planets 5 and 6 (hence 25 combinations). Each of these combinations has to be tested assuming that the transit at TJD = 2641.5778 belongs to the fifth planet and TJD = 2656.0944 belongs to the sixth planet (case A), and vice versa (case B). Fortunately, many of these 50 possibilities are excluded by existing data. We end up with four possibilities for case A and nine for case B. As seen in Fig. 2, all known chains of Laplace resonances have either their estimated generalized three-body Laplace angle $\Psi_{e=0}$ or their actual generalized three-body Laplace angle Ψ close to an equilibrium of the chain. We will hence favour the configurations that are closest to an equilibrium of the chain. For each case, the distance of each estimated angle to its closest equilibrium $\Delta\Psi = |\Psi_{e=0} - \Psi_{\mathrm{eq}}|$ is given in Extended Data Table 4. The case A2, with P_f/P_e = 4/3 and P_g/P_f = 4/3, comes out as a favourite, with the three outer generalized three-body Laplace angles at less than 20° from the closest equilibrium. Also, one can note that 4/3 MMRs are relatively common in resonant chains (see Supplementary Fig. 4).

For completeness, we study the role that the eccentricity of the orbit plays in the prediction. To estimate the generalized three-body Laplace angle

$$\Psi = l\lambda_1 - (l+m)\lambda_2 + m\lambda_3 \tag{1}$$

at a given epoch, we estimate the value of the λ_j as follows. Transits occur when the true longitude of the planet is equal to $l_0 = -\pi/2$. At first order in the eccentricity,

$$\lambda_0 = l_0 - 2e\sin(l_0 - \varpi) = -\frac{\pi}{2} + 2e\cos(\varpi). \tag{2}$$

We then assume the planet to be in a circular, unperturbed orbit to compute the value of its mean longitude at the time of transit t_0, $\lambda_0 = -\pi/2$. We hence obtain

$$\lambda(t) = -\frac{\pi}{2} + \frac{(t-t_0)}{P}2\pi. \tag{3}$$

The error on Ψ made by assuming zero eccentricity is hence, at first order[111]

$$|\Psi - \Psi_{e=0}| = |2le_1\cos\varpi_1 - 2(l+m)e_2\cos\varpi_2 + 2me_3\cos\varpi_3|. \tag{4}$$

This error can thus be substantial (several tens of degrees) if the eccentricities are on the order of several parts per hundred, as is the case for Kepler-223 (ref. 110). Therefore, we study whether a given combination of the eccentricities and longitudes of periastron can make $\Psi_{e=0}$ closer to the equilibrium than Ψ actually is, or vice versa. We check this for the cases presented in Extended Data Table 4.

Each case sets the orbital period of the planets and their mid-transit time. We estimate the planetary masses using the mass–radius relation from ref. 26. Then, varying the remaining parameters $k_i = e_i\cos\varpi_i$ and $h_i = e_i\sin\varpi_i$, we minimize the cost function

$$C = \mathcal{A}(\Psi_{\mathrm{bcd}}) + \mathcal{A}(\Psi_{\mathrm{cde}}) + \mathcal{A}(\Psi_{\mathrm{def}}) + \mathcal{A}(\Psi_{\mathrm{efg}}) \tag{5}$$

over 200 years, in which $\mathcal{A}(\Psi) = 2\pi$ if Ψ circulates and $\mathcal{A}(\Psi)$ is the peak-to-peak amplitude of libration of Ψ otherwise. For each case, 40 MCMC runs are conducted to minimize C, using REBOUND[113] for the N-body integration and samsam[114] for the MCMC. For each run, the k_i and h_i parameters are randomly initialized in the [−0.05, 0.05] range, which are also their boundaries during the MCMC runs. This allows eccentricities that are comparable with those of Kepler-60 (ref. 115) and Kepler-223 (ref. 110), which are other known chains for which the inner planets are far enough from the star to not have their eccentricities damped by tides.

The best solution of each fit is shown in Extended Data Fig. 3. Case A2 is the only one for which the best solutions consistently have a peak-to-peak amplitude of the generalized three-body Laplace angles

below 50° on average across the four angles. In all other cases, we were not able to find values of the k_i and k_j parameters below 85° of amplitude on average, with the exception of case A0, for which an average of about 66° was reached. The best solutions found across all MCMC runs for the A2 and A0 cases integrated for 1,000 years of evolution are shown in Supplementary Fig. 5. This analysis shows that the A2 case remains the one with the highest potential of being close to an equilibrium, while showing that all other cases cannot have an amplitude of libration smaller than 66° on average across their generalized three-body Laplace angles, regardless of the values of the k_i and k_j parameters. The case A2, with $P_f/P_e = 4/3$ and $P_g/P_f = 4/3$, is hence our prediction for the outer architecture of the HD 110067 system.

Confirming the predictions. Recovering the missing cadences of TESS Sector 23 observations. On the basis of the dynamical analysis presented above, the probable orbital periods associated with the two mono transits observed in TESS Sector 49 are approximately 41.05 and 54.74 days, respectively. According to this prediction, both planets transited their host star during TESS Sector 23 observations, but at a time when the photometry was highly affected by scattered light and sky background contamination. The Earth was a notable source of scattered light at the beginning of both Sector 23 orbits (TJD = 1928.09 and TJD = 1941.83) and the Moon was a notable source of scattered light for a few days after the beginning of the second orbit (between 1942 and 1947 TJD). The cadences affected were flagged by SPOC, thus not leaving enough valid data to derive cotrending basis vectors and missing in the PDCSAP light curve.

Our custom extraction using the PLD method from the section 'TESS photometry' was able to recover the missing data, showing two mono transits at 1943.6 and 1944.1 TJD (Fig. 1 and also Supplementary Fig. 6). Using MonoTools, we confirmed that the transits were consistent in duration–depth space with the two mono transits from TESS Sector 49 and separated by an integer number of orbits that matched the orbital periods predicted in our dynamical analysis for planets f and g. With this data reduction, all six planets in the HD 110067 system have been detected in transit at least twice, allowing a precise orbital period determination if we impose priors based on the hypothesis that all planets are trapped in a chain of first-order MMRs. Furthermore, we recovered an extra transit of planet b at the beginning of TESS Sector 23 observations.

Modelling of the ground-based photometric campaign. Targeted observations of HD 110067 were carried out on the night of 23 May 2022 to attempt to confirm the 41.05-day orbit of HD 110067 f as predicted through our resonance chain analysis. To reveal whether a transit was present in the combined dataset, we built a combined photometric model using all ground-based observations. To remove spurious systematic trends in a way that does not bias any transit fit, we opted to perform simultaneous linear decorrelation of each photometric dataset using the various metadata time series available. In all cases, for example, we included an air mass term in the decorrelation as well as a measure of the FWHM width. We also included two position-centroid terms (for MuSCAT2 and MuSCAT3), information on comparison star total counts and FWHM width (for LCO, Tierras and SAINT-EX), and interpolated colour time series derived from the relative shift in flux across bands in the MuSCAT2 and MuSCAT3 filters (as used in ref. 49). In all cases, the metadata were normalized to a time series with $\mu = 0$, $\sigma = 1$ and modelled using a single scaling parameter with a normal prior of $\mu = 0$, $\sigma = 0.5$. Quadratic limb-darkening parameters were also constrained using normal priors dictated by theoretical limb-darkening parameters as computed for each of the nine passbands using LDTK[116] and with inflated uncertainties following the methodology of the space-based photometric analysis. Each of the four time series observed by MuSCAT3 was split into two around an observing gap that occurred owing to the star passing close to the zenith at 06:57UT 24 May 2022. Individual time series were used for each of the nine NGTS telescopes, which were decorrelated independently. The final result is 24 individual photometric time series. An offset was also applied to each light curve, as well as a single global slope parameter to include the possibility of stellar activity.

The transit parameters were constrained on the basis of those found in a fit of the TESS Sector 49 mono transit. The predicted period used was $4/3 \times P_e = 41.051 \pm 0.1$ days, with the uncertainty implying a divergence from the perfect integer period of 2.4×10^{-3}—larger than those values found for the inner three planets. We limited the period to 41.0 ± 0.2 days to ensure a transit fit that could be explored with the temporal baseline of the photometry. Owing to the non-continuous nature of the photometry, the probability density function of the observed transit time is probably asymmetric and could potentially have several minima. Therefore, analyses using classical sampling techniques (MCMC, Hamiltonian Monte Carlo etc.) may not reveal the full picture. To initially test this, we kept all other parameters equal but split the range of periods covered by the time series into 36 bins across the anticipated period range ($40.8 < P < 41.2$) and fitted a constrained model for each. This would allow us to see the variation in the goodness-of-the-fit as a function of transit epoch. The transit model was built with exoplanet[99] and optimized using pymc3 (ref. 117), specifically with the pymc3-ext sampling, which enabled correlated parameters for each time series to be grouped together, speeding up the computation. To assess whether or not a transit model was justified over a flat model, we used the WAIC[118,119], as implemented in arviz[120].

Our results show a preference for a transit at the expected period $P = 41.04 \pm 0.01$ days, with a ΔWAIC of 9.5 over a transit-free model, as can be seen in Extended Data Fig. 4. Most instruments showed a weak preference for a peak at $P \approx 41.05$ days, with the exception of LCO (which observed no in-transit data) and SAINT-EX (which is the most affected by cirrus). This is only equivalent to moderate evidence for a roughly 41.051-day period of HD 110067 f. The lower two panels of Extended Data Fig. 4 show that both models (with or without transit) fit reasonably well. This is in part because systematic effects dominate over astrophysical signals for transits with depths below 1,000 ppm, especially when the target star is observed at a low air mass. A further peak in the WAIC is seen at about 40.9 days, but this hypothetical transit is covered only by the initial 1 h of MuSCAT2 photometry and does not fit our predicted period, hence we consider it spurious. This campaign shows that such transits are at the very limit of what is possible with ground-based observations. However, observations during a more favourable observing season and without technical issues such as the meridian flip of MuSCAT3 (which, unluckily, coincided with the expected egress) may have constrained better the presence of a transit.

Modelling of the radial velocity data. We carried out an initial frequency-based exploration of the CARMENES and HARPS-N spectroscopic datasets to see which substantial signals are present and those related to stellar activity using periodograms[121]. Supplementary Figs. 7 and 8 show that the dominant signal in the generalized Lomb–Scargle periodograms of both the radial velocities and main activity indicators (CCF-FWHM, differential line width, Mount Wilson's S-index, Hα emission) is attributable to the rotational period of the star, measured photometrically to be approximately 20 days using TESS and CHEOPS data. As well known, stellar activity induces spurious radial velocity signals (for example, refs. 122–125), which should be properly removed to unveil induced Keplerian motions in the star. We followed two independent approaches to model the data and minimize the impact of stellar activity effects on the detection and mass determination of the planets in the system.

Method I: SN-fit and breakpoint algorithm

Spurious radial velocity signals induced by stellar activity come from the line-shape variations in stellar spectra. Those can be quantified through the FWHM and the asymmetry of the cross-correlation function (CCF) computed from the spectra (for example, refs. 126–128). Following ref. 129, we first fit skew normal (SN) functions to the CCFs

available from HARPS-N and CARMENES. An SN function is not only characterized by a location and a scale parameter (which are the counterparts of the mean and standard deviation of a Gaussian) but it has a further free parameter that expresses its skewness (hereafter denoted with γ). For each observation, through the SN-fit, we were able to retrieve the stellar radial velocity ($\overline{\mathrm{RV}}$, quantified through the SN median), the $\mathrm{FWHM_{SN}}$, the contrast A and the asymmetry γ. The errors σ_{RV} of the $\overline{\mathrm{RV}}$ measurements were inferred using a bootstrap approach. Denoting with f_{CCF} the flux of a CCF data point, each point was perturbed by sampling values from a normal distribution whose standard deviation is equal to $\sqrt{f_{\mathrm{CCF}}}$, as the errors affecting the CCF data points are expected to be Poissonian.

After that, we applied the breakpoint method[130] to both the HARPS-N and CARMENES radial velocity time series. The algorithm has been designed to detect those locations along the radial velocity time series at which the correlation changes against the vector [$\mathrm{FWHM_{SN}}$, A, γ] are statistically significant. The goal is to then detrend the radial velocity time series by applying a piecewise interpolation to each segment found by the breakpoint algorithm rather than performing an overall correction to the whole time series. In this way, we are able to better correct for the contamination of stellar variability as shown by refs. 130,131. Finally, we jointly analysed the radial velocity time series using the MCMCI code[132], in which we switched off the interaction with stellar evolutionary models to speed up the computations. We set up the detrending function on each piecewise stationary segment found by the breakpoint algorithm as a polynomial of the following form

$$\begin{aligned}\mathrm{RV}_\star = \beta_0 + \sum_{k=1}^{k_t} \beta_{k,t} t^k + \sum_{k=1}^{k_F} \beta_{k,F} \mathrm{FWHM}_{\mathrm{SN}}^k + \sum_{k=1}^{k_A} \beta_{k,A} A^k + \\ + \sum_{k=1}^{k_\gamma} \beta_{k,\gamma} \gamma^k + \sum_{k=1}^{k_R} \beta_{k,R} \log R'_{\mathrm{HK}}{}^k ,\end{aligned} \tag{6}$$

in which (k_t, k_F, k_A, k_γ, k_R) is the vector of the polynomial orders whose optimal value has been established by launching several MCMC preliminary runs and selecting the combination that produces the minimum Bayesian information criterion (BIC)[133].

After performing a longer MCMCI run composed of four independent runs (300,000 steps each), which successfully converged as checked through the Gelman–Rubin test[134], we retrieved the posterior distributions of the system parameters. Their median values along with their error bars at the 1σ level are reported in Supplementary Tables 2 and 3. The full radial velocity time series and the phase-folded radial velocities of those planets whose detection is above the 3σ level (planets d and f) are shown in Supplementary Fig. 9.

Method II: multidimensional GP

On the other hand, we also perform a multidimensional Gaussian process (GP) approach to characterize the stellar and planetary signals in our radial velocity time series, as in refs. 135,136. This approach has proven useful to disentangle stellar and planetary signals in multiplanet systems (for example, refs. 137,138). We create N-dimensional GP models, including N time series $\mathcal{A}_i$, as

$$\begin{aligned}\mathcal{A}_1 &= A_1 G(t) + B_1 \dot{G}(t) \\ &\vdots \\ \mathcal{A}_N &= A_N G(t) + B_N \dot{G}(t),\end{aligned} \tag{7}$$

in which the variables $A_1, B_1, \ldots, A_N, B_N$, are free parameters that relate the individual time series to $G(t)$ and $\dot{G}(t)$. In this approach, $G(t)$ is assumed to be a latent (unobserved) variable that represents the projected area of the visible stellar disk that is covered by active regions as a function of time.

We model the stellar signal using a GP whose covariance between two times t_i and t_j is given by

$$\gamma_{\mathrm{QP},i,j} = \exp\left[-\frac{\sin^2[\pi(t_i - t_j)/P_{\mathrm{GP}}]}{2\lambda_{\mathrm{p}}^2} - \frac{(t_i - t_j)^2}{2\lambda_{\mathrm{e}}^2}\right], \tag{8}$$

in which $\gamma_{\mathrm{QP},i,j}$ is the quasiperiodic kernel, whose hyperparameters are, P_{GP}, the GP characteristic period, λ_{p}, the inverse of the harmonic complexity and λ_{e}, the long-term evolution timescale.

We perform a two-dimensional GP model between the radial velocities and the FWHM. We note that these quantities are equivalent in the HARPS-N and CARMENES data. The multidimensional covariance matrix was created using the kernel given in equation (8) and its derivatives[135,136]. We assume that radial velocities can be described as $\mathcal{A}_i = A_i G(t) + B_i \dot{G}(t)$, whereas the FWHM time series is described as $\mathcal{A}_i = A_i G(t)$. The planetary signals were included in the model as the mean function of the radial velocity time series. We use N Keplerian signals (in which N is the number of planetary signals), each one of them depending on the time of minimum conjunction t_0, orbital period P and Doppler semiamplitude K. All orbits are fixed to be circular, so the eccentricity and angle of periastron are fixed. For the FWHM, the mean function was treated as an offset, noting that we include a different offset per instrument. We also include a jitter term per time series and per instrument to account for unaccounted systematic errors.

We perform MCMC samplings of the parameter space using the code pyaneti (refs. 136,139). We sample the parameter space with 250 walkers and create the posterior distributions with the last 5,000 iterations of converged chains with a thin factor of 10. This leads to posterior distributions of 125,000 points for each sampled parameter. Figure 2 shows the spectroscopic time series resulting from this joint analysis. Median values along with their 1σ uncertainties are reported in Supplementary Table 4.

Modelling techniques using GP are particularly subject to overfitting, given their flexibility to reproduce (see, for example, refs. 140,141). To test the robustness of our GP model, we carried out a cross-validation analysis. We repeat the two-dimensional GP model described in this section but applied only to the HARPS-N data. Then, we create a predictive model with the inferred parameters and overlay the CARMENES data with median offsets subtracted (similar to a training/evaluation set for machine learning algorithms). Supplementary Fig. 10 shows this analysis, zoomed in to the 2021 observing campaign. The plot shows that the radial velocity data are in agreement with the predictive model, suggesting that our assumption that the stellar signal imprinted in the radial velocities can be described with a two-dimensional GP is valid for the time span of our observations. For the CCF FWHM CARMENES data, the correlation with the radial velocity measurements is not as strong as for the HARPS-N data, thus the prediction is less accurate in this case.

Both of these methods clearly detect planets HD 110067 d and f, and method II also detects planet b. However, the detection levels differ slightly. Recalling that the two different techniques are based on different radial velocity extraction methodologies and on different treatments of stellar activity, on the one hand, the slight output tension suggests that the radial velocity data alone do not strongly constrain all six Keplerian signals. We tested further stellar mitigation approaches, such as sinusoid fitting at the stellar rotation period and its harmonics or GP decorrelation as a function of time only, but they were all unsuccessful at constraining the masses of any of the planets (only the time-dependent GP model could recover the signal of planet f but with a much larger uncertainty, $K_{\mathrm{f}} = 2.0 \pm 1.0$ m s^{-1}). On the other hand, the radial velocity semiamplitudes inferred from the two methods are compatible within about 1.5σ, with the statistical tension $\Delta_{\mathrm{I\text{-}II}}$ below 1σ for planets b, c, d and g. Extended Data Fig. 5 shows the pairs of posterior density functions for the radial velocity semiamplitudes of each planet for comparison.

For HD 110067 f, after imposing a Gaussian prior centred around 41.05 days in both methods I and II radial velocity models, we indeed recover a substantial radial velocity signal with a detection level of

approximately 3σ. The planet transits only twice in the TESS data and the ground-based photometric campaign hints at moderate evidence for a planetary transit compatible with this value. Therefore, to secure an independent detection of planet f from spectroscopy, we performed a radial-velocity-only analysis imposing a uniform unbounded prior (between 30 and 54 days) to the orbital period. The MCMC converged and detected a clear Keplerian signal with a period $P_{f,uni} = 40.2 \pm 0.2$ days. Thus, the radial velocity data independently suggest the presence of a putative planet having a period close to 41.05 days. The tension at the approximately 4σ level with the predictions from the resonant chain model and the transit observations prove that the current radial velocity dataset cannot fully constrain the entire architecture of the planetary system.

Finally, we checked whether there are further Keplerian signals in the radial velocity time series. In particular, given that both planets e and g were not detected through our previous radial velocity analyses in which model-dependent values of the orbital periods were imposed as priors, we investigated the presence of potential planetary signals at different periods that could be attributed to planets e or g. To this end, we performed an MCMC run, in which we modelled planets b and c (which are clearly confirmed by the transit events) along with planets d and f (which are clearly detected also in the radial velocity time series). As a result, we produced the generalized Lomb–Scargle periodograms[121] of the residuals, obtained after subtracting the Keplerian signals of all four planets from the activity-cleaned time series (Supplementary Fig. 11). The high false-alarm probability level of the highest peak in both the HARPS-N (18%) and CARMENES (10%) residuals suggests that there are no signals left in the radial velocity data that could be associated with other planets or a misidentification of the orbital periods of planets e and g.

Final model. We computed a final model of the photometric and spectroscopic datasets of the HD 110067 system. On the basis of the analyses above, neither the light curves nor the radial velocities are precise enough to constrain the eccentricity of the planets. Assuming circular orbits, the photometry and radial velocity thus only constrain jointly the period and phase of a given planet in the system. However, the transit data dominate the precision of these two quantities (by several orders of magnitude). Therefore, for our final model, we opt to perform an independent analysis of the photometry and radial velocity datasets, in which priors inform the planet periods and phases in the radial velocity model based on the posterior distributions of the photometry-only fit. Besides, the large number of free parameters in each of the models makes it computationally expensive to run a joint fit, not to mention the complications for numerical samplers to explore the vast multidimensional parameter space. Table 1 shows the most relevant planetary parameters of the system based on the photometric fit from Supplementary Table 1, the radial velocity fit using method II from Supplementary Table 4 and the stellar parameters from Extended Data Table 3. A corner plot with the posterior distribution of the fitted transit parameters is shown in Supplementary Fig. 12. The resulting best-fit models and corresponding credibility bands are presented in Fig. 1 for the TESS and CHEOPS photometry and in Fig. 2 for the radial velocities.

Planetary internal structures. Using a Bayesian analysis[142,143], we computed the possible internal structures of the six planets of the system, using the results provided in Table 1, Extended Data Table 3 and the planetary masses from methods I and II. The forward model used to compute the likelihood is based on a four-layer structure: a central core (iron and sulfur), a silicate mantle (containing Si, Mg and Fe), a water layer and a gas layer (H and He). The equation of state (EOS) of water is the one in ref. 144, the core EOS is the one in ref. 145 and we use the EOS in ref. 146 for the silicate mantle. The thickness of the gas envelope, which depends on the planetary age, mass etc., is derived from ref. 147. Note that the influence of the gas layer on the innermost planet (compression and thermal effect) is not included in our model, as the mass of the gas layer for the six planets is small (see below). The planetary Si/Mg/Fe molar ratio in all planets is assumed to be equal to the stellar one. The prior distribution of the mass fractions of the three innermost layers (core, mantle and water layer) is assumed to be uniform on the simplex—the surface defined by the sum of the three mass fractions equal to one. Also, the mass fraction of the water layer is assumed to be 50% at most[148,149], and for the gas mass, we use a uniform log prior.

The results from this analysis are shown in Extended Data Fig. 6. Our model shows that the gas mass content of all planets is on the order $10^{-3}M_{\oplus}$ to $10^{-1}M_{\oplus}$ (median value, see Supplementary Table 5), with the notable exception of HD 110067 e (median value of about $10^{-7}M_{\oplus}$ using the masses from method I, approximately $10^{-3}M_{\oplus}$ using method II). The apparent lack of an atmosphere of planet e (located just outside planet d, which is the most gas-rich of the system, according to the internal structure models) is puzzling. If confirmed by future better determination of its density, the origin of the peculiar internal structure of planet e will have to be understood in the context of the very fragile architecture of the whole HD 110067 system. On the other hand, the water fraction for all planets is essentially unconstrained, owing to the still large uncertainty in the planetary masses. However, according to simulations of combined planetary formation and evolution, independently of the accretion mechanism (planetesimal-based or pebble-based), all the planets in the system have masses and radii consistent with a formation beyond the ice line[150–152]. Therefore, it is possible that, even though the water content is unconstrained in our model, the cores of the planets are rich in volatiles. JWST observations of some atmospheric trace gases (particularly ammonia, methane and/or methanol) could be used as a proxy for the presence of a deep or shallow surface that could break the degeneracies from internal composition models using bulk density measurements alone[153,154].

Data availability

The TESS observations used in this study are publicly available at the Mikulski Archive for Space Telescopes (https://archive.stsci.edu/missions-and-data/tess). The CHEOPS observations used in this study are available at the CHEOPS mission archive (https://cheops-archive.astro.unige.ch/archive_browser/). The ground-based photometry and high-resolution imaging observations are uploaded to ExoFOP (https://exofop.ipac.caltech.edu/tess/target.php?id=347332255) and are publicly available. CARMENES and HARPS-N reduced spectra, together with the derived CCF-based radial velocities and spectral indicators, are available at Zenodo (https://doi.org/10.5281/zenodo.8211589). All reduced transit photometry and radial velocity measurements used in this work are also provided at Zenodo (https://doi.org/10.5281/zenodo.8211589).

Code availability

We used the following publicly available codes, resources and Python packages to reduce, analyse and interpret our observations of HD 110067: numpy (ref. 155), matplotlib (ref. 156), astropy (ref. 157), lightkurve (ref. 44), PIPE (ref. 51,52), AstroImageJ (ref. 58), raccoon (ref. 73), serval (ref. 74), ARES (refs. 79,80), MOOG (ref. 81), ZASPE (ref. 83), emcee (ref. 158), CLES (ref. 96), exoplanet (ref. 99), MonoTools (ref. 106), pymc3 (ref. 117), ArviZ (ref. 120), GLS (ref. 121), MCMCI (ref. 132) and pyaneti (refs. 136,139). We can share the code used in the data reduction or data analysis on request.

27. Stassun, K. G. et al. The TESS input catalog and candidate target list. *Astron. J.* **156**, 102 (2018).
28. Stumpe, M. C. et al. Kepler Presearch Data Conditioning I—architecture and algorithms for error correction in Kepler light curves. *Proc. Acad. Sci. Pac.* **124**, 985 (2012).

29. Stumpe, M. C. et al. Multiscale systematic error correction via wavelet-based bandsplitting in Kepler data. *Proc. Acad. Sci. Pac.* **126**, 100 (2014).
30. Smith, J. C. et al. Kepler Presearch Data Conditioning II - a Bayesian approach to systematic error correction. *Proc. Acad. Sci. Pac.* **124**, 1000 (2012).
31. Jenkins, J. M. The impact of solar-like variability on the detectability of transiting terrestrial planets. *Astrophys. J.* **575**, 493–505 (2002).
32. Jenkins, J. M. et al. in *Software and Cyberinfrastructure for Astronomy* (eds Radziwill, N. M. & Bridger, A.) 77400D (SPIE, 2010).
33. Jenkins, J. M. et al. Kepler Data Processing Handbook: Transiting Planet Search. Kepler Science Document KSCI-19081-003 (2020).
34. Twicken, J. D. et al. Kepler data validation I—architecture, diagnostic tests, and data products for vetting transiting planet candidates. *Proc. Acad. Sci. Pac.* **130**, 064502 (2018).
35. Li, J. et al. Kepler data validation II-transit model fitting and multiple-planet search. *Proc. Acad. Sci. Pac.* **131**, 024506 (2019).
36. Guerrero, N. M. et al. The TESS Objects of Interest Catalog from the TESS Prime Mission. *Astrophys. J. Suppl. Ser.* **254**, 39 (2021).
37. Fausnaugh, M. M., Burke, C. J., Ricker, G. R. & Vanderspek, R. Calibrated full-frame images for the TESS Quick Look Pipeline. *Res. Notes AAS* **4**, 251 (2020).
38. Hedges, C. et al. TOI-2076 and TOI-1807: two young, comoving planetary systems within 50 pc identified by TESS that are ideal candidates for further follow up. *Astron. J.* **162**, 54 (2021).
39. Osborn, H. et al. Two warm Neptunes transiting HIP 9618 revealed by TESS & Cheops. *Mon. Not. R. Astron. Soc.* **523**, 3069–3089 (2023).
40. Vanderburg, A. et al. TESS spots a compact system of super-Earths around the naked-eye star HR 858. *Astrophys. J. Lett.* **881**, L19 (2019).
41. Deming, D. et al. Spitzer secondary eclipses of the dense, modestly-irradiated, giant exoplanet HAT-P-20b using pixel-level decorrelation. *Astrophys. J.* **805**, 132 (2015).
42. Luger, R. et al. EVEREST: pixel level decorrelation of K2 light curves. *Astron. J.* **152**, 100 (2016).
43. Luger, R. et al. starry: analytic occultation light curves. *Astron. J.* **157**, 64 (2019).
44. Lightkurve Collaboration et al. Lightkurve: Kepler and TESS time series analysis in Python. Astrophysics Source Code Library, record ascl:1812.013 (2018).
45. Gilliland, R. L. et al. Kepler mission stellar and instrument noise properties. *Astrophys. J. Suppl. Ser.* **197**, 6 (2011).
46. Van Cleve, J. E. et al. That's how we roll: the NASA K2 mission science products and their performance metrics. *Proc. Acad. Sci. Pac.* **128**, 075002 (2016).
47. Schanche, N. et al. TOI-2257 b: a highly eccentric long-period sub-Neptune transiting a nearby M dwarf. *Astron. Astrophys.* **657**, A45 (2022).
48. Ulmer-Moll, S. et al. Two long-period transiting exoplanets on eccentric orbits: NGTS-20 b (TOI-5152 b) and TOI-5153 b. *Astron. Astrophys.* **666**, A46 (2022).
49. Osborn, A. et al. TOI-431/HIP 26013: a super-Earth and a sub-Neptune transiting a bright, early K dwarf, with a third RV planet. *Mon. Not. R. Astron. Soc.* **507**, 2782–2803 (2021).
50. Tuson, A. et al. TESS and CHEOPS discover two warm sub-Neptunes transiting the bright K-dwarf HD 15906. *Mon. Not. R. Astron. Soc.* **523**, 3090–3118 (2023).
51. Szabó, G. M. et al. The changing face of AU Mic b: stellar spots, spin-orbit commensurability, and transit timing variations as seen by CHEOPS and TESS. *Astron. Astrophys.* **654**, A159 (2021).
52. Morris, B. M. et al. CHEOPS precision phase curve of the Super-Earth 55 Cancri e. *Astron. Astrophys.* **653**, A173 (2021).
53. Hoyer, S. et al. Expected performances of the Characterising Exoplanet Satellite (CHEOPS). III. Data reduction pipeline: architecture and simulated performances. *Astron. Astrophys.* **635**, A24 (2020).
54. Narita, N. et al. MuSCAT2: four-color simultaneous camera for the 1.52-m Telescopio Carlos Sánchez. *J. Astron. Telesc. Instrum. Syst.* **5**, 015001 (2019).
55. Parviainen, H. et al. MuSCAT2 multicolour validation of TESS candidates: an ultra-short-period substellar object around an M dwarf. *Astron. Astrophys.* **633**, A28 (2020).
56. Brown, T. M. et al. Las Cumbres Observatory global telescope network. *Proc. Acad. Sci. Pac.* **125**, 1031 (2013).
57. McCully, C. et al. in *Software and Cyberinfrastructure for Astronomy V* (eds Guzman, J. C. & Ibsen, J.) 107070K (2018).
58. Collins, K. A., Kielkopf, J. F., Stassun, K. G. & Hessman, F. V. AstroImageJ: image processing and photometric extraction for ultra-precise astronomical light curves. *Astron. J.* **153**, 77 (2017).
59. Wheatley, P. J. et al. The Next Generation Transit Survey (NGTS). *Mon. Not. R. Astron. Soc.* **475**, 4476–4493 (2018).
60. Garcia-Mejia, J. et al. in *Ground-based and Airborne Telescopes VIII* (eds Marshall, H. K., Spyromilio, J. & Usuda, T.) 114457R (SPIE, 2020).
61. Demory, B. O. et al. A super-Earth and a sub-Neptune orbiting the bright, quiet M3 dwarf TOI-1266. *Astron. Astrophys.* **642**, A49 (2020).
62. Narita, N. et al. in *Ground-based and Airborne Instrumentation for Astronomy VIII* (eds Evans, C. J., Bryant, J. J. & Motohara, K.) 114475K (SPIE, 2020).
63. Fukui, A. et al. Measurements of transit timing variations for WASP-5b. *Pub. Astron. Soc. Jpn.* **63**, 287–300 (2011).
64. Ciardi, D. R., Beichman, C. A., Horch, E. P. & Howell, S. B. Understanding the effects of stellar multiplicity on the derived planet radii from transit surveys: implications for Kepler, K2, and TESS. *Astrophys. J.* **805**, 16 (2015).
65. Hayward, T. L. et al. PHARO: a near-infrared camera for the Palomar Adaptive Optics System. *Proc. Acad. Sci. Pac.* **113**, 105–118 (2001).
66. Dekany, R. et al. PALM-3000: exoplanet adaptive optics for the 5 m Hale telescope. *Astrophys. J.* **776**, 130 (2013).
67. Furlan, E. et al. The Kepler follow-up observation program. I. A catalog of companions to Kepler stars from high-resolution imaging. *Astron. J.* **153**, 71 (2017).
68. Scott, N. J. et al. Twin high-resolution, high-speed imagers for the Gemini telescopes: instrument description and science verification results. *Front. Astron. Space Sci.* **8**, 138 (2021).
69. Howell, S. B., Everett, M. E., Sherry, W., Horch, E. & Ciardi, D. R. Speckle camera observations for the NASA Kepler Mission Follow-up Program. *Astron. J.* **142**, 19 (2011).
70. Mugrauer, M. & Michel, K.-U. Gaia search for stellar companions of TESS Objects of Interest. *Astron. Nachr.* **341**, 996–1030 (2020).
71. Mugrauer, M. & Michel, K.-U. Gaia search for stellar companions of TESS Objects of Interest II. *Astron. Nachr.* **342**, 840–864 (2021).
72. Ziegler, C. et al. SOAR TESS survey. I. Sculpting of TESS planetary systems by stellar companions. *Astron. J.* **159**, 19 (2020).
73. Lafarga, M. et al. The CARMENES search for exoplanets around M dwarfs. Radial velocities and activity indicators from cross-correlation functions with weighted binary masks. *Astron. Astrophys.* **636**, A36 (2020).
74. Zechmeister, M. et al. Spectrum radial velocity analyser (SERVAL). High-precision radial velocities and two alternative spectral indicators. *Astron. Astrophys.* **609**, A12 (2018).
75. Cosentino, R. et al. in *Ground-based and Airborne Instrumentation for Astronomy V* (eds Ramsay, S. K., McLean, I. S. & Takami, H.) 91478C (SPIE, 2014).
76. Santos, N. C. et al. SWEET-Cat: a catalogue of parameters for Stars With ExoplanETs. I. New atmospheric parameters and masses for 48 stars with planets. *Astron. Astrophys.* **556**, A150 (2013).
77. Sousa, S. G. *ARES + MOOG: A Practical Overview of an Equivalent Width (EW) Method to Derive Stellar Parameters* 297–310 (Springer, 2014).
78. Sousa, S. G. et al. SWEET-Cat 2.0: The Cat just got SWEETer. Higher quality spectra and precise parallaxes from Gaia eDR3. *Astron. Astrophys.* **656**, A53 (2021).
79. Sousa, S. G., Santos, N. C., Israelian, G., Mayor, M. & Monteiro, M. J. P. F. G. A new code for automatic determination of equivalent widths: Automatic Routine for line Equivalent widths in stellar Spectra (ARES). *Astron. Astrophys.* **469**, 783–791 (2007).
80. Sousa, S. G., Santos, N. C., Adibekyan, V., Delgado-Mena, E. & Israelian, G. ARES v2: new features and improved performance. *Astron. Astrophys.* **577**, A67 (2015).
81. Sneden, C. A. *Carbon and Nitrogen Abundances in Metal-Poor Stars*. PhD thesis, Univ. Texas at Austin (1973).
82. Kurucz, R. L. SYNTHE spectrum synthesis programs and line data. Astrophysics Source Code Library (1993).
83. Brahm, R., Jordán, A., Hartman, J. & Bakos, G. ZASPE: a code to measure stellar atmospheric parameters and their covariance from spectra. *Mon. Not. R. Astron. Soc.* **467**, 971–984 (2017).
84. Adibekyan, V. Zh. et al. Chemical abundances of 1111 FGK stars from the HARPS GTO planet search program. Galactic stellar populations and planets. *Astron. Astrophys.* **545**, A32 (2012).
85. Adibekyan, V. et al. Identifying the best iron-peak and α-capture elements for chemical tagging: the impact of the number of lines on measured scatter. *Astron. Astrophys.* **583**, A94 (2015).
86. Castelli, F. & Kurucz, R. L. in *Modelling of Stellar Atmospheres, Proc. 210th Symposium of the International Astronomical Union* (eds Piskunov, N., Weiss, W. W. & Gray, D. F.) A20 (Astronomical Society of the Pacific, 2003).
87. Allard, F. in *Exploring the Formation and Evolution of Planetary Systems, Proc. IAU Symposium No. 299* (eds Booth, M., Matthews, B. C. & Graham, J. R.) 271–272 (International Astronomical Union, 2014).
88. Blackwell, D. E. & Shallis, M. J. Stellar angular diameters from infrared photometry. Application to Arcturus and other stars; with effective temperatures. *Mon. Not. R. Astron. Soc.* **180**, 177–191 (1977).
89. Schanche, N. et al. WASP-186 and WASP-187: two hot Jupiters discovered by SuperWASP and SOPHIE with additional observations by TESS. *Mon. Not. R. Astron. Soc.* **499**, 428–440 (2020).
90. Wilson, T. G. et al. A pair of sub-Neptunes transiting the bright K-dwarf TOI-1064 characterized with CHEOPS. *Mon. Not. R. Astron. Soc.* **511**, 1043–1071 (2022).
91. Lindegren, L. et al. Gaia Early Data Release 3. Parallax bias versus magnitude, colour, and position. *Astron. Astrophys.* **649**, A4 (2021).
92. Bonfanti, A. et al. CHEOPS observations of the HD 108236 planetary system: a fifth planet, improved ephemerides, and planetary radii. *Astron. Astrophys.* **646**, A157 (2021).
93. Bonfanti, A., Ortolani, S., Piotto, G. & Nascimbeni, V. Revising the ages of planet-hosting stars. *Astron. Astrophys.* **575**, A18 (2015).
94. Bonfanti, A., Ortolani, S. & Nascimbeni, V. Age consistency between exoplanet hosts and field stars. *Astron. Astrophys.* **585**, A5 (2016).
95. Marigo, P. et al. A new generation of PARSEC-COLIBRI stellar isochrones including the TP-AGB phase. *Astrophys. J.* **835**, 77 (2017).
96. Scuflaire, R. et al. CLÉS, Code Liégeois d'Évolution Stellaire. *Astrophys. Space Sci.* **316**, 83–91 (2008).
97. Salmon, S. J. A. J., Van Grootel, V., Buldgen, G., Dupret, M. A. & Eggenberger, P. Reinvestigating α Centauri AB in light of asteroseismic forward and inverse methods. *Astron. Astrophys.* **646**, A7 (2021).
98. Reddy, B. E., Lambert, D. L. & Allende Prieto, C. Elemental abundance survey of the Galactic thick disc. *Mon. Not. R. Astron. Soc.* **367**, 1329–1366 (2006).
99. Foreman-Mackey, D. et al. dfm/exoplanet: exoplanet v0.2.1. Zenodo https://zenodo.org/record/3462740 (2019).
100. Delrez, L. et al. Transit detection of the long-period volatile-rich super-Earth ν^2 Lupi d with CHEOPS. *Nat. Astron.* **5**, 775–787 (2021).
101. Claret, A. A new method to compute limb-darkening coefficients for stellar atmosphere models with spherical symmetry: the space missions TESS, Kepler, CoRoT, and MOST. *Astron. Astrophys.* **618**, A20 (2018).
102. Claret, A. Limb and gravity-darkening coefficients for the Space Mission CHEOPS. *Res. Notes AAS* **5**, 13 (2021).
103. Van Eylen, V. & Albrecht, S. Eccentricity from transit photometry: small planets in Kepler multi-planet systems have low eccentricities. *Astrophys. J.* **808**, 126 (2015).
104. Xie, J.-W. et al. Exoplanet orbital eccentricities derived from LAMOST–Kepler analysis. *Proc. Natl Acad. Sci. USA* **113**, 11431–11435 (2016).
105. Hadden, S. & Lithwick, Y. Kepler planet masses and eccentricities from TTV analysis. *Astron. J.* **154**, 5 (2017).

106. Osborn, H. P. MonoTools: planets of uncertain periods detector and modeler. Astrophysics Source Code Library, record ascl:2204.020 (2022).
107. Kipping, D. The orbital period prior for single transits. *Res. Notes AAS* **2**, 223 (2018).
108. Van Eylen, V. et al. The orbital eccentricity of small planet systems. *Astron. J.* **157**, 61 (2019).
109. Osborn, H. P. et al. Uncovering the true periods of the young sub-Neptunes orbiting TOI-2076. *Astron. Astrophys.* **664**, A156 (2022).
110. Mills, S. M. et al. A resonant chain of four transiting, sub-Neptune planets. *Nature* **533**, 509–512 (2016).
111. Siegel, J. C. & Fabrycky, D. Resonant chains of exoplanets: libration centers for three-body angles. *Astron. J.* **161**, 290 (2021).
112. Lopez, T. A. et al. Exoplanet characterisation in the longest known resonant chain: the K2-138 system seen by HARPS. *Astron. Astrophys.* **631**, A90 (2019).
113. Rein, H. & Liu, S. F. REBOUND: an open-source multi-purpose N-body code for collisional dynamics. *Astron. Astrophys.* **537**, A128 (2012).
114. Delisle, J.-B. samsam: Scaled Adaptive Metropolis SAMpler. Astrophysics Source Code Library, record ascl:2207.011 (2022).
115. Leleu, A. et al. Removing biases on the density of sub-Neptunes characterised via transit timing variations. Update on the mass-radius relationship of 34 Kepler planets. *Astron. Astrophys.* **669**, A117 (2023).
116. Parviainen, H. & Aigrain, S. ldtk: Limb Darkening Toolkit. *Mon. Not. R. Astron. Soc.* **453**, 3821–3826 (2015).
117. Salvatier, J., Wiecki, T. V. & Fonnesbeck, C. Probabilistic programming in Python using PyMC3. *PeerJ Comput. Sci.* **2**, e55 (2016).
118. Watanabe, S. & Opper, M. Asymptotic equivalence of Bayes cross validation and widely applicable information criterion in singular learning theory. *J. Mach. Learn. Res.* **11**, 3571–3594 (2010).
119. Vehtari, A., Gelman, A. & Gabry, J. Practical Bayesian model evaluation using leave-one-out cross-validation and WAIC. *Stat. Comput.* **27**, 1413–1432 (2017).
120. ArviZ Developers. ArviZ: exploratory analysis of Bayesian models. Astrophysics Source Code Library, record ascl:2004.012 (2020).
121. Zechmeister, M. & Kürster, M. The generalised Lomb-Scargle periodogram. A new formalism for the floating-mean and Keplerian periodograms. *Astron. Astrophys.* **496**, 577–584 (2009).
122. Saar, S. H. & Donahue, R. A. Activity-related radial velocity variation in cool stars. *Astrophys. J.* **485**, 319–327 (1997).
123. Hatzes, A. P. Starspots and exoplanets. *Astron. Nachr.* **323**, 392–394 (2002).
124. Meunier, N., Desort, M. & Lagrange, A. M. Using the Sun to estimate Earth-like planets detection capabilities. II. Impact of plages. *Astron. Astrophys.* **512**, A39 (2010).
125. Dumusque, X., Boisse, I. & Santos, N. C. SOAP 2.0: a tool to estimate the photometric and radial velocity variations induced by stellar spots and plages. *Astrophys. J.* **796**, 132 (2014).
126. Queloz, D. et al. No planet for HD 166435. *Astron. Astrophys.* **379**, 279–287 (2001).
127. Boisse, I. et al. Stellar activity of planetary host star HD 189 733. *Astron. Astrophys.* **495**, 959–966 (2009).
128. Dumusque, X. Radial velocity fitting challenge. I. Simulating the data set including realistic stellar radial-velocity signals. *Astron. Astrophys.* **593**, A5 (2016).
129. Simola, U., Dumusque, X. & Cisewski-Kehe, J. Measuring precise radial velocities and cross-correlation function line-profile variations using a Skew Normal density. *Astron. Astrophys.* **622**, A131 (2019).
130. Simola, U. et al. Accounting for stellar activity signals in radial-velocity data by using change point detection techniques. *Astron. Astrophys.* **664**, A127 (2022).
131. Bonfanti, A. et al. TOI-1055 b: Neptunian planet characterised with HARPS, TESS, and CHEOPS. *Astron. Astrophys.* **671**, L8 (2023).
132. Bonfanti, A. & Gillon, M. MCMCI: a code to fully characterise an exoplanetary system. *Astron. Astrophys.* **635**, A6 (2020).
133. Schwarz, G. Estimating the dimension of a model. *Ann. Stat.* **6**, 461–464 (1978).
134. Gelman, A. & Rubin, D. B. Inference from iterative simulation using multiple sequences. *Stat. Sci.* **7**, 457–472 (1992).
135. Rajpaul, V., Aigrain, S., Osborne, M. A., Reece, S. & Roberts, S. A Gaussian process framework for modelling stellar activity signals in radial velocity data. *Mon. Not. R. Astron. Soc.* **452**, 2269–2291 (2015).
136. Barragán, O., Aigrain, S., Rajpaul, V. M. & Zicher, N. PYANETI - II. A multidimensional Gaussian process approach to analysing spectroscopic time-series. *Mon. Not. R. Astron. Soc.* **509**, 866–883 (2022).
137. Barragán, O. et al. The young HD 73583 (TOI-560) planetary system: two 10-$M_{\oplus}$ mini-Neptunes transiting a 500-Myr-old, bright, and active K dwarf. *Mon. Not. R. Astron. Soc.* **514**, 1606–1627 (2022).
138. Zicher, N. et al. One year of AU Mic with HARPS – I. Measuring the masses of the two transiting planets. *Mon. Not. R. Astron. Soc.* **512**, 3060–3078 (2022).
139. Barragán, O., Gandolfi, D. & Antoniciello, G. PYANETI: a fast and powerful software suite for multiplanet radial velocity and transit fitting. *Mon. Not. R. Astron. Soc.* **482**, 1017–1030 (2019).
140. Cale, B. L. et al. Diving beneath the sea of stellar activity: chromatic radial velocities of the young AU Mic planetary system. *Astron. J.* **162**, 295 (2021).
141. Blunt, S. et al. Overfitting affects the reliability of radial velocity mass estimates of the V1298 Tau planets. *Astron. J.* **166**, 62 (2023).
142. Dorn, C. et al. Can we constrain the interior structure of rocky exoplanets from mass and radius measurements? *Astron. Astrophys.* **577**, A83 (2015).
143. Dorn, C. et al. A generalized Bayesian inference method for constraining the interiors of super Earths and sub-Neptunes. *Astron. Astrophys.* **597**, A37 (2017).
144. Haldemann, J., Alibert, Y., Mordasini, C. & Benz, W. AQUA: a collection of H_2O equations of state for planetary models. *Astron. Astrophys.* **643**, A105 (2020).
145. Hakim, K. et al. A new ab initio equation of state of hcp-Fe and its implication on the interior structure and mass-radius relations of rocky super-Earths. *Icarus* **313**, 61–78 (2018).
146. Sotin, C., Grasset, O. & Mocquet, A. Mass radius curve for extrasolar Earth-like planets and ocean planets. *Icarus* **191**, 337–351 (2007).
147. Lopez, E. D. & Fortney, J. J. Understanding the mass–radius relation for sub-Neptunes: radius as a proxy for composition. *Astrophys. J.* **792**, 1 (2014).
148. Thiabaud, A. et al. From stellar nebula to planets: the refractory components. *Astron. Astrophys.* **562**, A27 (2014).
149. Marboeuf, U., Thiabaud, A., Alibert, Y., Cabral, N. & Benz, W. From planetesimals to planets: volatile molecules. *Astron. Astrophys.* **570**, A36 (2014).
150. Venturini, J., Guilera, O. M., Haldemann, J., Ronco, M. P. & Mordasini, C. The nature of the radius valley. Hints from formation and evolution models. *Astron. Astrophys.* **643**, L1 (2020).
151. Emsenhuber, A. et al. The New Generation Planetary Population Synthesis (NGPPS). II. Planetary population of solar-like stars and overview of statistical results. *Astron. Astrophys.* **656**, A70 (2021).
152. Izidoro, A. et al. The exoplanet radius valley from gas-driven planet migration and breaking of resonant chains. *Astrophys. J.* **939**, L19 (2022).
153. Hu, R. et al. Unveiling shrouded oceans on temperate sub-Neptunes via transit signatures of solubility equilibria versus gas thermochemistry. *Astrophys. J.* **921**, L8 (2021).
154. Tsai, S.-M. et al. Inferring shallow surfaces on sub-Neptune exoplanets with JWST. *Astrophys. J.* **922**, L27 (2021).
155. Harris, C. R. et al. Array programming with NumPy. *Nature* **585**, 357–362 (2020).
156. Hunter, J. D. Matplotlib: a 2D graphics environment. *Comput. Sci. Eng.* **9**, 90–95 (2007).
157. The Astropy Collaboration et al. The Astropy Project: sustaining and growing a community-oriented open-source project and the latest major release (v5.0) of the core package. *Astrophys. J.* **935**, 167 (2022).
158. Foreman-Mackey, D., Hogg, D. W., Lang, D. & Goodman, J. emcee: the MCMC hammer. *Proc. Acad. Sci. Pac.* **125**, 306 (2013).
159. MacDonald, M. G., Shakespeare, C. J. & Ragozzine, D. A five-planet resonant chain: reevaluation of the Kepler-80 system. *Astron. J.* **162**, 114 (2021).
160. Cannon, A. J. & Pickering, E. C. The Henry Draper catalogue 0h, 1h, 2h, and 3h. *Ann. Harvard College Observatory* **91**, 1–290 (1918).
161. Gaia Collaboration et al. Gaia Early Data Release 3. Summary of the contents and survey properties. *Astron. Astrophys.* **649**, A1 (2021).
162. Yoss, K. M. & Griffin, R. F. Radial velocities and DDO, BV photometry of Henry Draper G5-M stars near the North Galactic Pole. *J. Astrophys. Astron.* **18**, 161–227 (1997).
163. Skrutskie, M. F. et al. The Two Micron All Sky Survey (2MASS). *Astron. J.* **131**, 1163–1183 (2006).
164. Delisle, J. B. Analytical model of multi-planetary resonant chains and constraints on migration scenarios. *Astron. Astrophys.* **605**, A96 (2017).

Acknowledgements We acknowledge the use of public TESS data from pipelines at the TESS Science Office and at the TESS Science Processing Operations Center (SPOC). Resources supporting this work were provided by the NASA High-End Computing (HEC) Program through the NASA Advanced Supercomputing (NAS) Division at Ames Research Center for the production of the SPOC data products. The CHaracterising ExOPlanets Satellite (CHEOPS) is a European Space Agency (ESA) mission in partnership with Switzerland with important contributions to the payload and the ground segment from Austria, Belgium, France, Germany, Hungary, Italy, Portugal, Spain, Sweden and the United Kingdom. The CHEOPS Consortium would like to gratefully acknowledge the support received by all the agencies, offices, universities and industries involved. Their flexibility and willingness to explore new approaches were essential to the success of this mission. CARMENES acknowledges financial support from the Agencia Estatal de Investigación of the Ministerio de Ciencia e Innovación MCIN/AEI/10.13039/501100011033 and the European Regional Development Fund (ERDF) 'A way of making Europe' through projects PID2019-107061GB-C61, PID2019-107061GB-C66, PID2021-125627OB-C31 and PID2021-125627OB-C32, from the Centre of Excellence 'Severo Ochoa' award to the Instituto de Astrofísica de Canarias (IAC; CEX2019-000920-S), from the Centre of Excellence 'María de Maeztu' award to the Institut de Ciències de l'Espai (CEX2020-001058-M) and from the Generalitat de Catalunya/CERCA programme. Based on observations made with the Italian Telescopio Nazionale Galileo (TNG) operated on the island of La Palma by the Fundación Galileo Galilei of the Istituto Nazionale di Astrofisica (INAF) at the Spanish Observatorio del Roque de los Muchachos of the Instituto de Astrofisica de Canarias. This article is based on observations made with the MuSCAT2 instrument, developed by the Astrobiology Center (ABC), at Telescopio Carlos Sánchez operated on the island of Tenerife by the IAC in the Spanish Observatorio del Teide. This paper is based on observations made with the MuSCAT3 instrument, developed by ABC and under financial supports by JSPS KAKENHI (JP18H05439) and JST PRESTO (JPMJPR1775), at Faulkes Telescope North on Maui, Hawaii, operated by the Las Cumbres Observatory. Tierras is supported by grants from the John Templeton Foundation and the Harvard Origins of Life Initiative. The opinions expressed in this publication are those of the authors and do not necessarily reflect the views of the John Templeton Foundation. The Next Generation Transit Survey (NGTS) facility is operated by the consortium institutes with support from the UK Science and Technology Facilities Council (STFC) under projects ST/M001962/1 and ST/S002642/1. Some of the observations presented in this paper were carried out at the Observatorio Astronómico Nacional on the Sierra de San Pedro Mártir (OAN-SPM), Baja California, México. This work makes use of observations from the Las Cumbres Observatory global telescope network. Some of the observations in this paper made use of the High-Resolution Imaging instrument Alopeke and were obtained under Gemini LLP Proposal Number GN-S-2021A-LP-105. Alopeke was funded by the NASA Exoplanet Exploration Program and built at the NASA Ames Research Center by S. B. Howell, N. Scott, E. P. Horch and E. Quigley. Alopeke was mounted on the Gemini North telescope of the international Gemini Observatory, a programme of NSF OIR Lab, which is managed by the Association of Universities for Research in Astronomy (AURA) under a cooperative agreement with the National Science Foundation. On behalf of the Gemini partnership: the National Science Foundation (United States), National Research Council (Canada), Agencia Nacional de Investigación y Desarrollo (Chile), Ministerio de Ciencia, Tecnología e Innovación (Argentina), Ministério da Ciência, Tecnologia, Inovações e Comunicações (Brazil) and Korea Astronomy and Space Science Institute (Republic of Korea). This work was supported by the KESPRINT collaboration, an international consortium devoted to the characterization and research of exoplanets discovered with space-based missions. R.Lu. thanks D. Fabrycky for helpful

discussions about the orbital dynamics of the HD110067 system. R.Lu. acknowledges funding from University of La Laguna through the Margarita Salas Fellowship from the Spanish Ministry of Universities ref. UNI/551/2021-May 26 and under the EU Next Generation funds. This work has been carried out within the framework of the National Centre for Competence in Research (NCCR) PlanetS supported by the Swiss National Science Foundation (SNSF) under grants 51NF40_182901 and 51NF40_205606. A.C.Ca. and T.G.Wi. acknowledge support from STFC consolidated grant numbers ST/R000824/1 and ST/V000861/1 and UKSA grant number ST/R003203/1. O.Ba. acknowledges funding from the European Research Council (ERC) under the European Union's Horizon 2020 research and innovation programme (grant agreement no. 865624). M.Le. acknowledges support of the SNSF under grant number PCEFP2_194576. P.F.L.Ma. acknowledges support from STFC research grant number ST/M001040/1. Y.Al. acknowledges support from the SNSF under grant 200020_192038. D.Ga. gratefully acknowledges financial support from the CRT foundation under grant no. 2018.2323 'Gaseous or rocky? Unveiling the nature of small worlds'. J.A.Eg. acknowledges support from the SNSF under grant 200020_192038. G.No. is grateful for the research funding from the Ministry of Education and Science programme 'The Excellence Initiative – Research University' conducted at the Centre of Excellence in Astrophysics and Astrochemistry of the Nicolaus Copernicus University in Torun, Poland. D.Ra. was supported by NASA under award number NNA16BD14C for NASA Academic Mission Services. M.La. acknowledges funding from a UKRI Future Leader Fellowship, grant number MR/S035214/1. V.Ad. is supported by Fundação para a Ciência e a Tecnologia (FCT) through national funds by grants UIDB/04434/2020, UIDP/04434/2020 and 2022.06962.PTDC. P.J.Am. acknowledges financial support from grants CEX2021-001131-S and PID2019-109522GB-C52, both funded by MCIN/AEI/ 10.13039/501100011033 and by the ERDF 'A way of making Europe'. S.C.C.Ba. acknowledges support from FCT through FCT contract no. IF/01312/2014/CP1215/CT0004. X.Bo., S.Ch., D.Ga., M.Fr. and J.La. acknowledge their role as ESA-appointed CHEOPS science team members. L.Bo., V.Na., I.Pa., G.Pi., R.Ra., G.Sc., and T.Zi. acknowledge support from CHEOPS ASI-INAF agreement no. 2019-29-HH.0. A.Br. was supported by the Swedish National Space Agency (SNSA). Contributions at the Mullard Space Science Laboratory by E.M.Br. were supported by STFC through the consolidated grant ST/W001136/1. S.C.-G. acknowledges support from UNAM PAPIIT-IG101321. D.Ch. and J.G.-M. thank the staff at the F. L. Whipple Observatory for their assistance in the refurbishment and maintenance of the 1.3-m telescope. W.D.Co. acknowledges support from NASA grant 80NSSC23K0429. This is University of Texas Center for Planetary Systems Habitability Contribution 0063. K.A.Co. acknowledges support from the TESS mission through subaward s3449 from MIT. H.J.De. acknowledges support from the Spanish Research Agency of the Ministry of Science and Innovation (AEI-MICINN) under grant PID2019-107061GB-C66, doi:10.13039/501100011033. This project was supported by the CNES. The Belgian participation to CHEOPS has been supported by the Belgian Federal Science Policy Office (BELSPO) in the framework of the PRODEX Program and by the University of Liège through an ARC grant for Concerted Research Actions financed by the Wallonia-Brussels Federation. L.De. is an F.R.S.-FNRS Postdoctoral Researcher. This work was supported by FCT through national funds and by FEDER through COMPETE2020 – Programa Operacional Competitividade e Internacionalizacão by these grants: UID/FIS/04434/2019, UIDB/04434/2020, UIDP/04434/2020, PTDC/FIS-AST/32113/2017 and POCI-01-0145-FEDER-032113, PTDC/FIS-AST/28953/2017 and POCI-01-0145-FEDER-028953, PTDC/FIS-AST/28987/2017 and POCI-01-0145-FEDER-028987. O.D.S.De. is supported in the form of work contract (DL 57/2016/CP1364/CT0004) funded by national funds through FCT. B.-O.De. acknowledges support from the Swiss State Secretariat for Education, Research and Innovation (SERI) under contract number MB22.00046. This project has received funding from the ERC under the European Union's Horizon 2020 research and innovation programme (project Four Aces grant agreement no. 724427). It has also been carried out in the frame of the NCCR PlanetS supported by the SNSF. D.Eh. acknowledges financial support from the SNSF for project 200021_200726. E.E.-B. acknowledges financial support from the European Union and the State Agency of Investigation of the Spanish Ministry of Science and Innovation (MICINN) under the grant PRE2020-093107 of the Pre-Doc Program for the Training of Doctors (FPI-SO) through FSE funds. M.Fr. gratefully acknowledges the support of the Swedish National Space Agency (DNR 65/19, 174/18). J.G.-M. acknowledges support by the National Science Foundation through a Graduate Research Fellowship under grant no. DGE1745303 and by the Ford Foundation through a Ford Foundation Predoctoral Fellowship, administered by the National Academies of Sciences, Engineering, and Medicine. The contributions at the University of Warwick by S.Gi. have been supported by STFC through consolidated grants ST/L000733/1 and ST/P000495/1. M.Gi. is F.R.S.-FNRS Research Director. Y.G.M.Ch. acknowledges support from UNAM PAPIIT-IG101321. E.Go. acknowledges support by the Thueringer Ministerium füër Wirtschaft, Wissenschaft und Digitale Gesellschaft. M.N.Gu. is the ESA CHEOPS Project Scientist and Mission Representative and, as such, is also responsible for the Guest Observers (GO) Programme. M.N.Gu. does not relay proprietary information between the GO and Guaranteed Time Observation (GTO) Programmes, and does not decide on the definition and target selection of the GTO Programme. A.P.Ha. acknowledges support by DFG grant HA 3279/12-1 within the DFG Schwerpunkt SPP 1992. Ch.He. acknowledges support from the European Union H2020-MSCA-ITN-2019 under grant agreement no. 860470 (CHAMELEON). S.Ho. gratefully acknowledges CNES funding through the grant 837319. This work is partly supported by JST CREST grant number JPMJCR1761. K.G.Is. is the ESA CHEOPS Project Scientist and is responsible for the ESA CHEOPS GO Programme. She does not participate in, or contribute to, the definition of the Guaranteed Time Programme of the CHEOPS mission through which observations described in this paper have been taken nor to any aspect of target selection for the programme. J.Ko. gratefully acknowledges the support of the SNSA (DNR 2020-00104) and of the Swedish Research Council (VR: Etableringsbidrag 2017-04945). K.W.F.La. was supported by Deutsche Forschungsgemeinschaft grants RA714/14-1 within the DFG Schwerpunkt SPP 1992, Exploring the Diversity of Extrasolar Planets. This work was granted access to the HPC resources of MesoPSL financed by the Region Ile de France and the project Equip@Meso (reference ANR-10-EQPX-29-01) of the programme Investissements d'Avenir supervised by the Agence Nationale pour la Recherche. A.L.desE. acknowledges support from the CNES (Centre national d'études spatiales, France). This work is partly supported by Astrobiology Center SATELLITE Research project AB022006. This work is partly supported by JSPS KAKENHI grant number JP18H05439 and JST CREST grant number JPMJCR1761. H.L.M.Os. acknowledges funding support by STFC through a PhD studentship. H.Pa. acknowledges the support by the Spanish Ministry of Science and Innovation with the Ramon y Cajal fellowship number RYC2021-031798-I. This work was also partially supported by a grant from the Simons Foundation (PI: Queloz, grant number 327127). S.N.Qu. acknowledges support from the TESS mission through subaward s3449 from MIT. S.N.Qu. acknowledges support from the TESS GI Program under award 80NSSC21K1056 (G03268). L.Sa. acknowledges support from UNAM PAPIIT project IN110122. N.C.Sa. acknowledges funding by the European Union (ERC, FIERCE, 101052347). Views and opinions expressed are, however, those of the author(s) only and do not necessarily reflect those of the European Union or the ERC. Neither the European Union nor the granting authority can be held responsible for them. N.Sc. acknowledges support from the SNSF (PP00P2-163967 and PP00P2-190080) and NASA under award number 80GSFC21M0002. S.G.So. acknowledges support from FCT through FCT contract no. CEECIND/00826/2018 and POPH/FSE (EC). Gy.M.Sz. acknowledges the support of the Hungarian National Research, Development and Innovation Office (NKFIH) grant K-125015, a PRODEX Experiment Agreement no. 4000137122, the Lendület LP2018-7/2021 grant of the Hungarian Academy of Science and the support of the city of Szombathely. A.Tu. acknowledges funding support from the STFC through a PhD studentship. V.V.Ey. acknowledges support by the STFC through the consolidated grant ST/W001136/1. V.V.Gr. is an F.R.S.-FNRS Research Associate. J.Ve. acknowledges support from the SNSF under grant PZ00P2_208945. N.A.Wa. acknowledges UKSA grant ST/R004838/1. N.Wa. is partly supported by JSPS KAKENHI grant number JP21K20376.

Author contributions R.Lu., H.P.Os., A.Le., E.Pa., A.Bo., O.Ba. and T.G.Wi. conceived the project and contributed notably to the writing of this manuscript. R.Lu. and H.P.Os. led the analysis of the photometric data. A.Le. led the dynamical analysis of the system and developed the method with J.-B.De. to predict the orbits of the planets based on their resonant state within the chain. R.Lu., A.Bo. and O.Ba. led the analysis of the radial velocity data and the stellar activity mitigation. T.G.Wi. led the stellar characterization with the help of V.Ad., S.G.So., A.Bo., V.V.Gr., S.Sa. and W.D.Co. Y.Al. and J.A.Eg. led the analysis of the internal structures and L.Fo. and A.Bo. performed the atmospheric evolution simulations. D.Ra., J.D.Tw. and J.M.Je. improved the TESS data reduction to recover the missing cadences affected by reflected light and high background. R.Lu., E.Pa. and G.No. planned and obtained the time for the observations with CARMENES and HARPS-N. CARMENES observations were made possible by M.La., J.C.Mo., P.J.Am., A.Qu. and I.Ri. HARPS-N observations were made possible by I.Ca., J.O.-M., F.Mu., H.J.De., J.Ko., D.Ga., J.H.Li., W.D.Co., E.W.Gu., V.V.Ey., H.L.M.Os., S.Re., E.Go., F.Da. and K.W.F.La. High-resolution imaging observations from Palomar and Gemini North were made possible by A.W.Bo., D.R.Ci., I.J.M.Cr., S.B.Ho., E.Ma. and J.E.Sc. Ground-based photometric observations to catch the transit of planet f were made possible by the MuSCAT2 (R.Lu., E.Pa., N.Na., J.H.Li., K.Ik., E.E.-B., J.O.-M., N.Wa., F.Mu., G.No., A.Fu., H.Pa., M.Mo., T.Ka., J.P.D.Le. and T.Ko.), LCO (T.G.Wi., R.Lu., H.P.Os., E.Pa., A.Le., A.Tu., M.J.Ho., Y.Al. and D.Ga.), NGTS (H.P.Os., S.Gi., D.Ba., D.R.An., M.Mo., A.M.S.Sm., E.M.Br. and S.Ud.), Tierras (J.G.-M. and D.Ch.), SAINT-EX (N.Sc., Y.G.M.Ch., L.Sa., S.C.-G. and B.-O.De.) and MuSCAT3 (N.Na., J.H.Li., K.Ik., N.Wa., A.Fu., M.Mo., T.Ka., J.P.D.Le. and T.Ko.) instruments. The remaining authors provided key contributions to the development of the TESS and CHEOPS mission. All authors read and commented on the manuscript and helped with its revision.

Competing interests The authors declare no competing interests.

Additional information

Supplementary information The online version contains supplementary material available at https://doi.org/10.1038/s41586-023-06692-3.

Correspondence and requests for materials should be addressed to R. Luque.

Peer review information *Nature* thanks Eric Agol and the other, anonymous, reviewer(s) for their contribution to the peer review of this work.

Reprints and permissions information is available at http://www.nature.com/reprints.

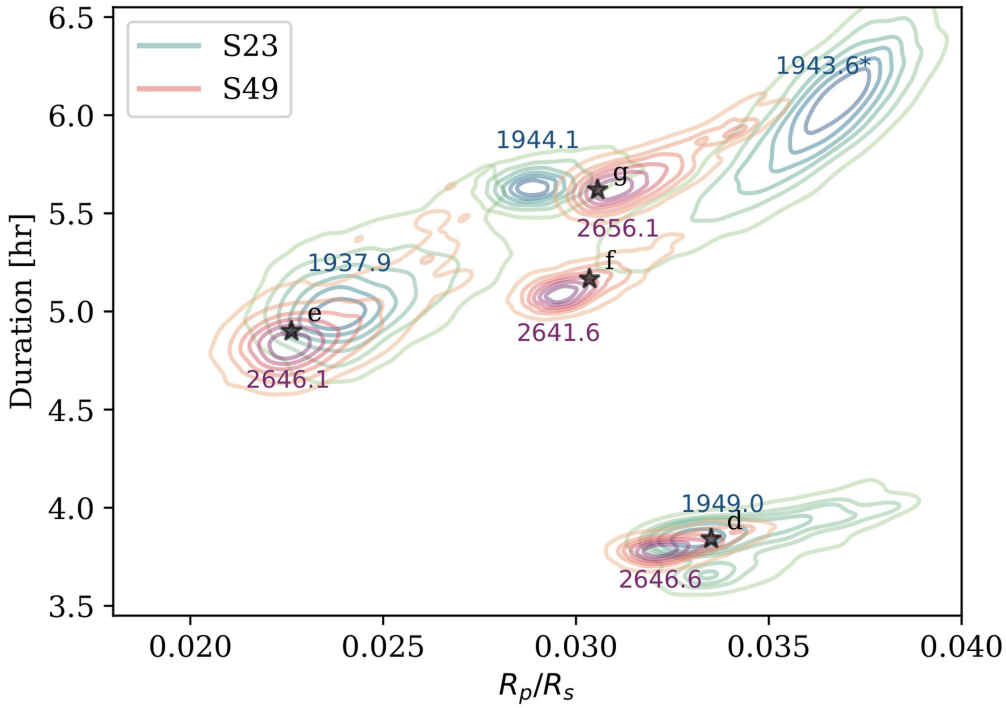

Extended Data Fig. 1 | Transit duration versus transit depth for all unassigned transits in the TESS data. TESS Sector 23 and Sector 49 are shown as different colours. The numbers above each transit denote the mid-transit time in TJD. Contours represent percentile levels, the innermost one corresponding to the 50th percentile and the outermost to the 99th percentile by increments of 10%. The transit of planet f in PLD photometry is marked with * to indicate that its properties are heavily affected by pretransit systematic noise.

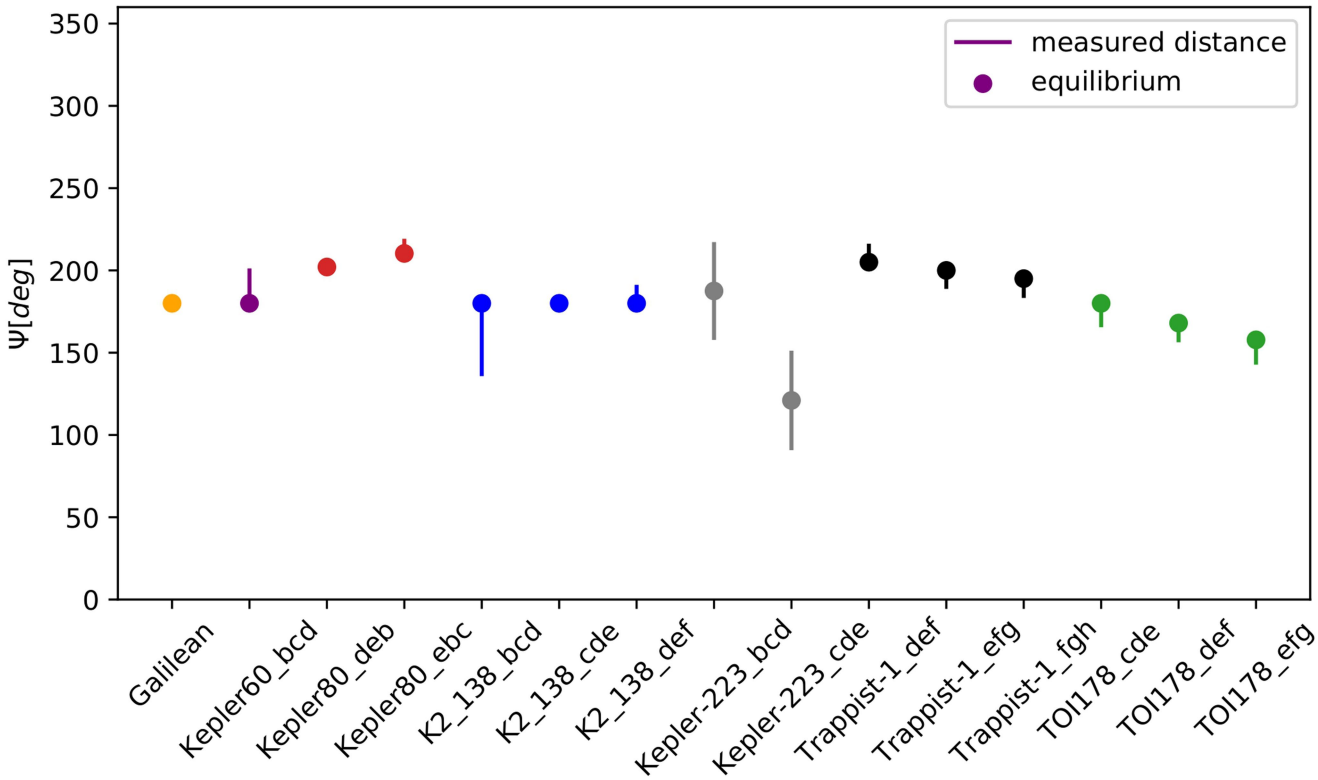

Extended Data Fig. 2 | Generalized three-body Laplace angles for known systems in resonant chains. Included are the Galilean satellites Kepler-60 (refs. 12,115), Kepler-80 (ref. 159), K2-138 (ref. 112), Kepler-223 (ref. 110), TRAPPIST-1 (ref. 13) and TOI-178 (ref. 10). Measurements belonging to the same system are marked with the same colour. The line marks the observed distance to the theorized equilibrium (marked with a circle). The distances are estimated at the zeroth order in eccentricity[110,111]. For most systems, a single estimation of the generalized Laplace angle is made, whereas ref. 110 made an estimation for each Kepler quarter.

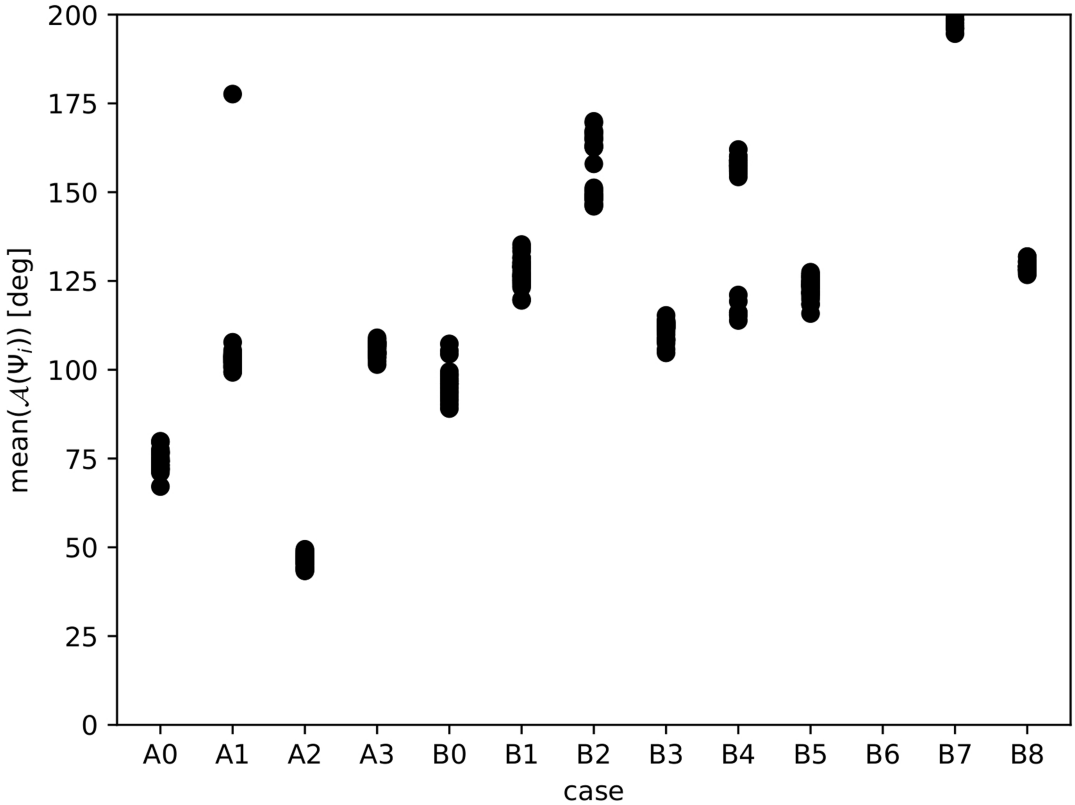

Extended Data Fig. 3 | Observed distance from the equilibrium for all the simulated scenarios in which planets f and g continue the resonant chain. The *y* axis is converted to the mean peak-to-peak amplitude from the generalized three-body Laplace angle using the following expression: mean ($\mathcal{A}(\Psi_i)$) = $C/4$. Case A2 remains the one that has the potential to be the closest to an equilibrium.

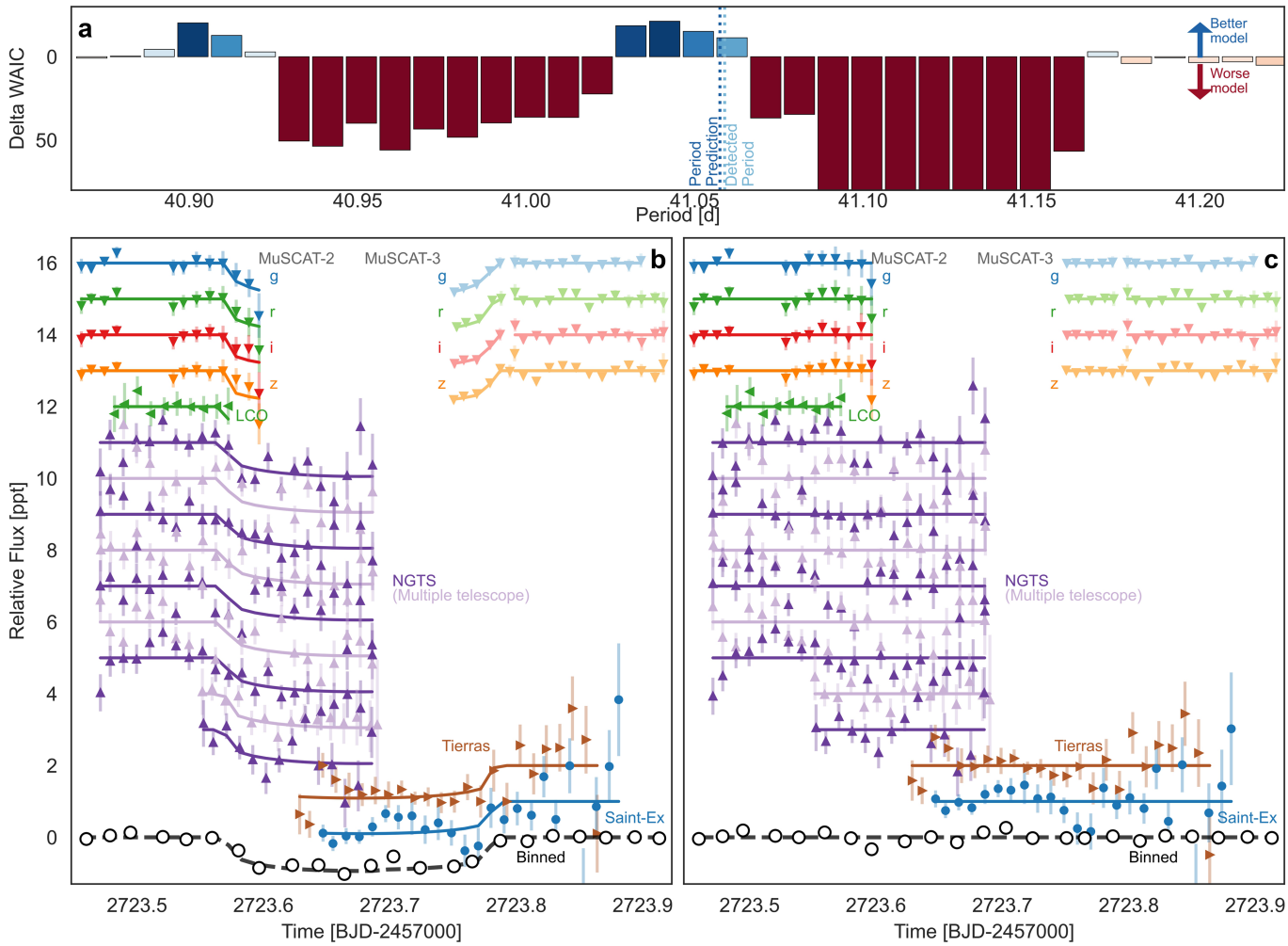

Extended Data Fig. 4 | Results from the ground-based campaign to detect HD 110067 f. a, ΔWAIC for each of the constrained period bins when compared with a transit-free model. **b**,**c**, Best-fit decorrelated photometry with (**b**) and without (**c**) a transit model. Each light curve from each telescope has been offset for clarity. Error bars represent 1σ uncertainties.

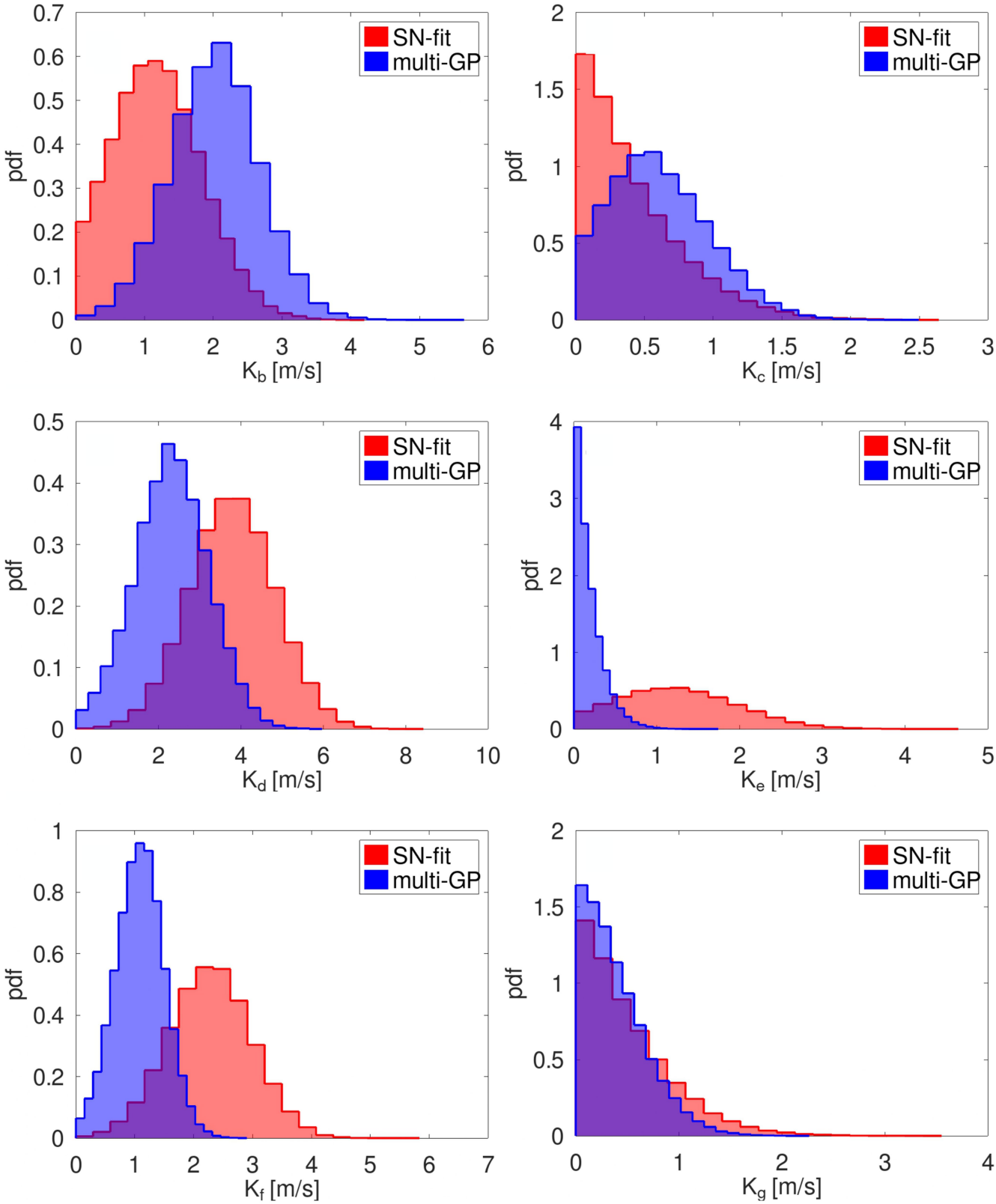

Extended Data Fig. 5 | Results from the two radial velocity analyses to measure the mass of each of the planets in the HD 110067 system. Each histogram represents the posterior density function (pdf) of the radial velocity semiamplitudes as inferred from method I (red) and method II (blue). The area underneath each histogram is normalized to unity.

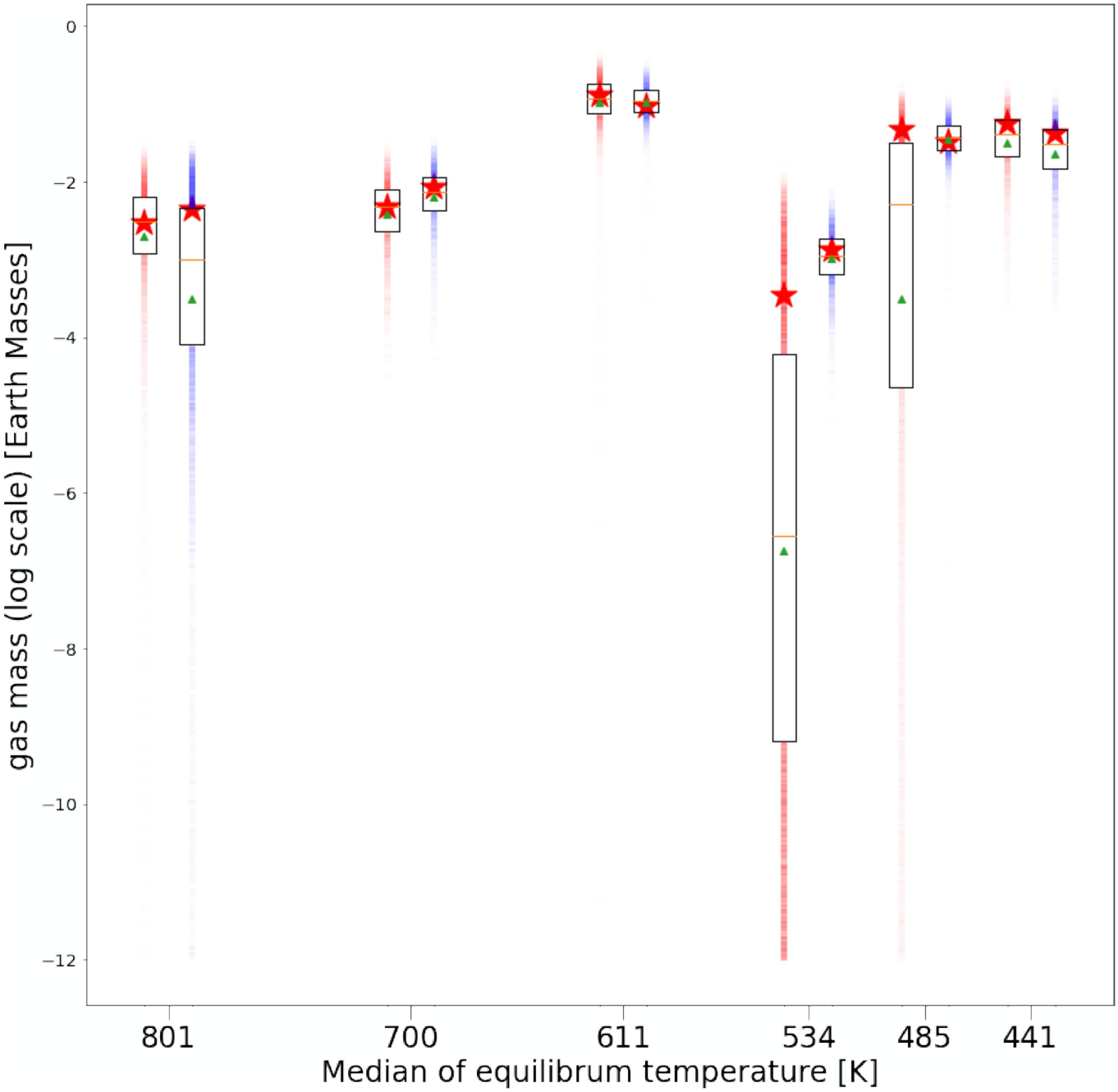

Extended Data Fig. 6 | Gas mass fraction of the HD 110067 planets as a function of their equilibrium temperature. We infer two values per planet by assuming the different planetary masses from our method I (red) and method II (blue) radial velocity analyses. The boxes, orange lines, green triangles and red stars represent, respectively, the 25th and 75th percentiles, medians, means and modes of the posterior distributions. The opacity of the vertical lines is proportional to the posterior distribution.

Extended Data Table 1 | CHEOPS observing log

Start (TJD)	Length [hr]	Archive filekey	Av. eff. (%)	RMS (ppm)	Notes
2681.3341	9.93	PR110048_TG025701_V0200	79	202	e, 35.4d alias
2683.1380	10.36	PR110048_TG025801_V0200	68	212	e, 37.3d alias
2685.2296	10.4	PR110048_TG025901_V0200	68	196	e, 39.3d alias
2690.0127	9.88	PR110048_TG026601_V0200	71	183	d, 21.8d alias
2692.9367	4.84	PR100031_TG052101_V0200	75	187	filler
2693.3133	5.27	PR100031_TG052102_V0200	60	217	filler
2694.6805	8.21	PR100031_TG052001_V0200	73	212	**Planet b**
2702.5843	9.26	PR110048_TG026701_V0200	72	220	d, 22.65d alias
2703.0623	10.36	PR110048_TG026101_V0200	61	217	d, 18.86d alias
2704.0525	9.34	PR110048_TG026801_V0200	62	213	d, 23.38d alias
2704.7545	3.2	PR110031_TG052201_V0200	71	251	filler
2706.1956	9.38	PR110048_TG026401_V0200	57	256	d, 19.93d alias
2707.9583	9.44	PR110048_TG028101_V0200	66	275	**Planet d**, 20.5d alias
2712.8885	8.37	PR100031_TG052002_V0200	61	240	**Planet b**
2713.9877	8.76	PR110048_TG028001_V0200	60	247	d, 22.5d alias
2714.4689	4.19	PR100031_TG052103_V0200	60	258	filler
2714.7439	10.08	PR110048_TG028501_V0200	61	249	d, 24.4d alias
2715.1871	3.06	PR100031_TG052202_V0200	52	222	filler
2717.2854	9.86	PR110048_TG028401_V0200	56	243	g, $2 \times P_e$

Filler observations aim to catch transits serendipitously in between time-critical observations with higher priority. Boldface notes indicate that a transit event was detected in the data.

Extended Data Table 2 | Ground-based photometric campaign observing log

Facility	Filter	Start (TJD)	End (TJD)	Notes
MuSCAT-2	g,r,i,z_s	2723.4534	2723.5991	Interrupted at 2723.488 for 54 min
LCO	z_p	2723.4797	2723.5756	No in-transit data at expected ingress
NGTS	custom	2723.4684	2723.6904	From 9 telescopes, 2 started late
Tierras	custom	2723.6260	2723.8681	Affected by cirrus
SAINT-EX	zcut	2723.6446	2723.8826	Affected by cirrus
MuSCAT-3	g,r,i,z_s	2723.7479	2723.9177	Interrupted at 2723.795 for 8 min
Transit	–	2723.5869	2723.7987	Expected in/egress for reference

Extended Data Table 3 | Stellar parameters of HD 110067

Parameter	Value	Reference
	Name and identifiers	
Name	HD 110067	[160]
TIC	347332255	[27]
TOI	1835	[36]
	Coordinates and spectral type	
α	12:39:21.503	[161]
δ	+20:01:40.03	[161]
Epoch	2000.0	[161]
Spectral type	K0.0 V	[162]
	Magnitudes	
B [mag]	9.203 ± 0.03	[162]
V [mag]	8.419 ± 0.002	[162]
G [mag]	8.17208 ± 0.00028	[161]
J [mag]	6.952 ± 0.023	[163]
H [mag]	6.561 ± 0.017	[163]
K_s [mag]	6.492 ± 0.018	[163]
	Parallax and kinematics	
π [mas]	31.037 ± 0.022	[161]
d [pc]	32.220 ± 0.023	[161]
$\mu_\alpha \cos\delta$ [mas yr^{-1}]	-81.96 ± 0.08	[161]
μ_δ [mas yr^{-1}]	-104.59 ± 0.04	[161]
U [km s^{-1}]	+7.50±0.01	This work
V [km s^{-1}]	-13.56±0.03	This work
W [km s^{-1}]	-4.06±0.20	This work
	Photospheric parameters	
$T_{\rm eff}$ [K]	5266 ± 64	This work
$\log g$	4.54 ± 0.03	This work
[Fe/H]	-0.20 ± 0.04	This work
[Mg/H]	-0.21 ± 0.06	This work
[Si/H]	-0.19 ± 0.03	This work
$v \sin i_\star$ [km s^{-1}]	2.5 ± 1.0	This work
	Physical parameters	
M [$M_\odot$]	0.798 ± 0.042	This work
R [$R_\odot$]	0.788 ± 0.008	This work
Age [Gyr]	8.1 ± 4.0	This work

Error bars represent 1σ uncertainties. See refs. 27,36,160–163.

Extended Data Table 4 | Distance of the estimated generalized three-body Laplace angle $\Psi_{e=0}$ to the closest equilibrium for all period ratios that are not excluded by available observations

Case	P_f/P_e	P_g/P_f	P_f (days)	P_g (days)	$\Delta\Psi_{bcd}$ (deg)	$\Delta\Psi_{cde}$ (deg)	$\Delta\Psi_{def}$ (deg)	$\Delta\Psi_{efg}$ (deg)	*
A0	4/3	2/1	41.0575	82.1150	44.17	18.55	7.67	95.50	1
A1	4/3	3/2	41.0575	61.5862	44.17	36.13	88.05	79.21	1
A2	4/3	4/3	41.0575	54.7433	44.17	18.06	4.89	9.81	1
A3	4/3	6/5	41.0575	49.2690	44.17	37.57	80.14	95.33	1
B0	2/1	2/1	61.5862	123.172	44.17	10.00	43.60	21.79	0
B1	2/1	3/2	61.5862	92.3793	44.17	10.00	43.60	106.64	0
B2	2/1	4/3	61.5862	82.1150	44.17	10.00	43.60	168.50	0
B3	2/1	6/5	61.5862	73.9035	44.17	10.00	43.60	1.21	0
B4	3/2	2/1	46.1897	92.3793	44.17	10.00	73.33	167.00	0
B5	3/2	6/5	46.1897	55.4276	44.17	10.00	73.33	100.43	0
B6	4/3	2/1	41.0575	82.1150	44.17	38.56	136.29	72.06	1
B7	4/3	4/3	41.0575	54.7433	44.17	38.07	133.51	177.37	1
B8	5/4	5/4	38.4914	48.1142	44.17	10.00	52.81	110.80	0

Case A assumes that the mono transit at 2641.5778 TJD belongs to the fifth planet and that at 2656.0944 TJD belongs to the sixth planet. Case B assumes the opposite. The flag column *=1 indicates that the position of the equilibria varies with the masses of the planets, in which case the equilibrium is recomputed using ref. 164, with masses computed using a mass–radius relation for sub-Neptunes[26]. For *=0, the equilibrium is 180°.